
Upconverting Lanthanide-doped Y_2O_3 Nanoparticles for Phototherapy

Synthesis, Morphology and Optical analysis.

Master Thesis by

Arend Zhang

Daily Supervisor: **Dechao Yu, Ph. D**

Project Supervisor: **Prof. Andries Meijerink**

Conducted at Condensed Matter and Interfaces (CMI) research group of the Debye Institute for
Nanomaterials Science

Faculty of Science at Utrecht University

Contents

Abstract	1
1. Introduction.....	2
1.1 Phototherapy	2
1.2 Local treatment solution.....	3
1.3 Lanthanide-doped upconverting nanoparticles.....	3
2. Theory	5
2.1 Luminescence.....	5
2.2 Lanthanides.....	6
2.3 Upconversion	9
2.4 Energy Transfer	11
2.5 Quenching pathways.....	13
2.6 Lifetime of photoluminescence	14
3. Experimental	15
3.1 Synthesis	15
3.1.1 Microcrystalline Y_2O_3	15
3.1.2 Nanocrystalline Y_2O_3	15
3.2 Characterization & Optical Spectroscopy	17
3.2.1 Crystal structure & Morphology	17
3.2.2 Optical properties & Upconversion	17
4. Results & Discussion.....	18
4.1 Microcrystalline Y_2O_3 : Er /Ho, Gd.....	18
4.1.1 XRD Results	19
4.1.2 Photoluminescence results.....	21
4.1.3 Time resolved measurements.....	30
4.1.4 Influence of calcination temperature	32
4.1.5 Summary & comparison.....	33
4.2 Nanocrystalline Y_2O_3 : 0.5% Ho, 10% Gd.....	34
4.2.1 Results of Method A (RE-Carbonates)	34
4.2.2 Results of Method B (RE-Chlorides)	36
4.2.3 Results of Method C (RE-Nitrates)	38
4.2.4 Optical results, summary & comparison.....	39
5. Conclusions & Outlook	41
6. Acknowledgements.....	42
7. References.....	43
8. Appendices.....	45

A.	Results of CW-laser measurements	45
B.	Excitation graphs of 1 & 3% Ho ³⁺ concentration.....	47
C.	TEM images of the NPs of Method B calcined at various temperatures	48

Abstract

Visible-to-UVB upconversion (UC) is a promising technique to treat skin diseases such as Psoriasis. In recent works, the lanthanide $\text{Ho}^{3+}\text{-Gd}^{3+}$ couple doped in the NaYF_4 host lattice resulted in successful blue-to-UVB UC emission from the Gd^{3+} ($^6\text{P}_{7/2}$) state. This can be used in a topical carrier to treat skin diseases resulting in cost-effective and time-efficient treatment. An alternative host lattice: Y_2O_3 (yttria) was tested in this work using the $\text{Ho}^{3+}\text{-Gd}^{3+}$ and $\text{Er}^{3+}\text{-Gd}^{3+}$ blue-to-UVB UC dopant couples. Yttria is known for its excellent thermal and chemical stability. For both lanthanide couples, microcrystalline doped yttria were successfully synthesized and blue-to-UVB UC was realized. Blue-to-UVB UC was furthermore achieved in the $\text{Ho}^{3+}\text{-Gd}^{3+}$ doped yttria nanocrystals. It was found that the efficiency of the blue-to-UVB UC of the yttria particles decreases significantly when the particles size is reduced to nanocrystalline. The presented work is the first to realize $\text{Ho}^{3+}\text{-Gd}^{3+}$ doped Y_2O_3 (~450 nm) blue-to-UVB (~313 nm) upconverting nanoparticles. Further research may help to enhance the UC efficiency.

1. Introduction

1.1 Phototherapy

Various skin diseases such as psoriasis and vitiligo are known to affect a significant fraction of the human population, worldwide numbers indicate an occurrence of about 1 to 3% for psoriasis and 1% for vitiligo.¹ An effective and well-known treatment for these diseases is phototherapy using narrowband ultraviolet-B radiation (NB-UVB, 311–313 nm).^{2,3} The reason behind this specific wavelength range is that NB-UVB radiation delivers optimal healing results with little side effects. It is well known that UV radiation can cause erythema (sun burn) but in the 311–313 nm wavelength range this is limited. In Figure 1.1 the action spectrum of erythema, beneficial spectrum of Psoriasis and a typical UV-B lamp spectrum are plotted.

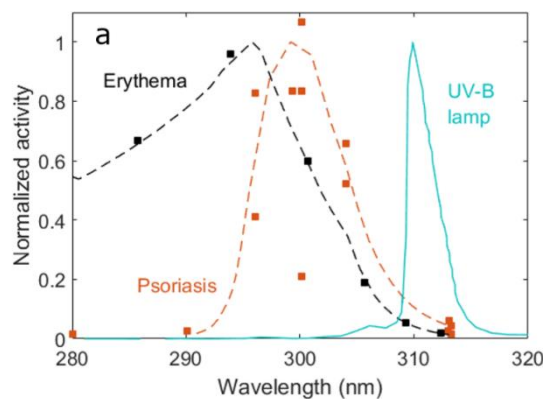


Figure 1.1: Action spectrum of erythema (sun burn) (black) and psoriasis (orange) with a typical spectrum of a UVB lamp for phototherapy (blue).

Nowadays, conventional phototherapy requires the patient to visit the clinic two to three times a week. This is impractical for some individuals as the treatment is both time consuming and costly.⁴ Phototherapy performed by the patient at home is in this case more practical, however, current commercially available NB-UVB emitting devices are expensive (> 3000 USD). In addition, there is the need to invest in educating the patient to prevent adverse reactions in case of wrong application. A side effect the conventional phototherapy is that the surrounding healthy skin gets exposed to NB-UVB which leads to increased risk of skin cancer.⁵ Blue light (~450 nm) treatment is known to be effective for treatment against psoriasis while having no known side effects but it is significantly less effective than with UVB for the treatment for most skin diseases.⁶ It can be concluded that the conventional phototherapy is an effective but demanding treatment method with potential side effects due to overexposure of healthy skin.

1.2 Local treatment solution

A solution to these problems was proposed which is illustrated in the schematic in Figure 1.2. The conventional phototherapy consists of a NB-UVB light source which is directly applied on the skin of the entire hand with the reddish spots being the affected area. This can generate overexposure of the healthy skin. In Figure 1.2 **b**, the proposed treatment shows a blue light source (~ 450 nm) being applied on the same area. In this case, the reddish areas are covered by a cream or a patch which consists of upconverting nanoparticles (NPs). These NPs can convert this blue light into NB-UVB which localizes the treatment. The utilization of this cream/ patch containing these UCNPs can solve many of the existing problems. The light source will be one that emits in the visible light spectrum and replaces the costly NB-UVB emitting light source. The treatment will be more accessible and less hazardous for the patient to perform at home since blue light is safe.⁶

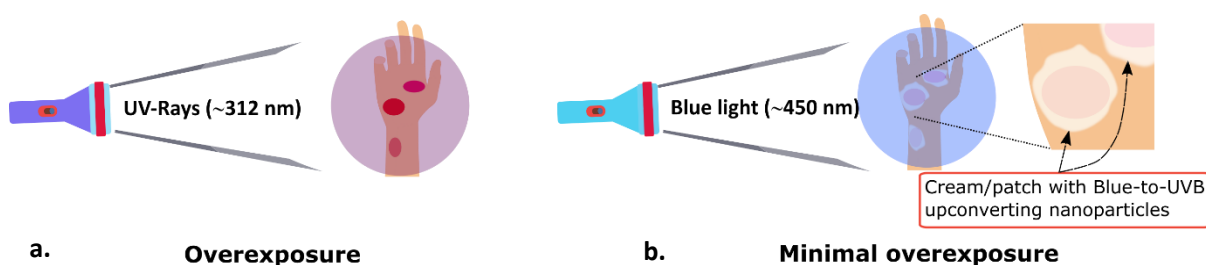


Figure 1.2: A schematic overview of on the left **a.** the conventional phototherapy setup, on the right **b.** the proposed localized treatment using a topical carrier which can be a cream or patch that contains Blue-to-UVB UCNP's.

1.3 Lanthanide-doped upconverting nanoparticles

Lanthanide-doped upconverting NPs are a class of inorganic crystalline materials that can convert both near-infrared (NIR) and visible (VIS) excitation into visible and ultraviolet (UV) emission. These special optical properties have already been used to improve numerous biological applications and offers new potential in photovoltaic and display technology.^{7,8} The basic mechanism of upconversion (UC) can be understood as converting two or more low energy excitation photons into one emitted photon of higher energy as schematically depicted in Figure 1.3.⁹ This example is only one of the many UC mechanisms which will be addressed in the theory section.

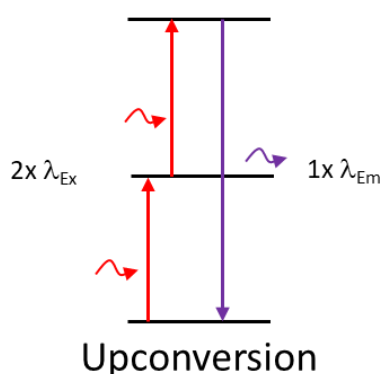


Figure 1.3: A schematic upconversion scheme where two lower energy photons are converted into one photon with higher energy.

An example of an extensively studied UC process is the conversion from near-infrared to the visible spectrum (NIR-to-VIS) with an application in anti-counterfeiting, optical labelling/ imaging in biological assays and luminescent temperature sensors for materials in the nanoscale regime.¹⁰ A substantial amount of research and work has already been done on NIR to VIS upconversion but hardly any on the specific upconversion of VIS-to-UVB.^{11, 9} In our group, this has already been achieved by co-doping the Ho^{3+} - Gd^{3+} lanthanide couple in NaYF_4 which has demonstrated the possibility of the application.

Exploration of the VIS-to-UVB UC in other host materials is limited. For this reason, in this project we investigate the Blue-to-UVB upconversion in another host material, Y_2O_3 , which will be doped with the Erbium-Gadolinium or Holmium-Gadolinium couple (Y_2O_3 : x% Er^{3+} / Ho^{3+} , y% Gd^{3+}). This host was chosen for its interesting physical properties, such as its chemical stability up to high temperatures (melting point of 2425°C), high mechanical strength, high thermal conductivity, large optical bandgap and high refractive index. These are excellent characteristics for the proposed medical treatment and could result into an even more efficient VIS-to-UVB UC as the UC efficiency is known to be host material dependent.^{12, 13}

The main challenge in this project is to synthesize nanocrystalline Y_2O_3 particles in the sub-100 nm range. This is known to be difficult in controlling the size and morphology due to the calcination process required after nanoparticles synthesis to make the NPs crystalline. The calcination process can easily lead to uncontrollable aggregation and growth of the NPs.¹⁴ The reason for synthesizing blue-to-UVB upconverting NPs is for the purpose of future work with dye-sensitization. This serves to enhance the absorption of blue (~450 nm) light because Lanthanides have weak absorptions.¹⁵ NPs have a larger surface area on which more dyes can be attached to (see Figure 1.4). Several synthesis methods will be used in trying to reach the goal of size controllable sub-100 nm Y_2O_3 NPs with VIS-to-UVB UC properties through incorporation of Ho^{3+} - Gd^{3+} and Er^{3+} - Gd^{3+} UV couples.

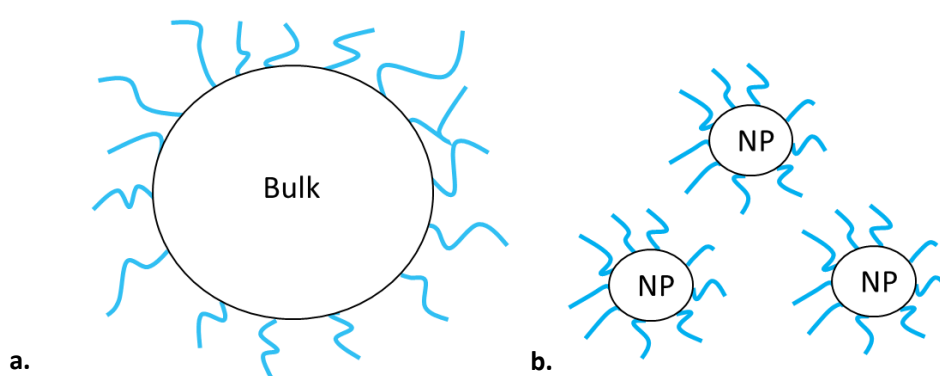


Figure 1.4: Depiction of future work of dye-binding the blue-to-UVB UC particles to enhance the absorption efficiency. In the bulk material (a.) there is less surface than the NPs (b.) which leads to less dye ligands to attach to the surface compared to NPs.

2. Theory

An understanding of the fundamentals of various theoretical subjects involved in luminescence is required to appreciate the results reported in this thesis. Thus, this chapter will provide the reader with relevant and practical information to more easily comprehend the results and discussions in the following chapters.

2.1 Luminescence

Luminescent materials, also known as phosphors, can be found in most light sources. They are implemented in many everyday applications such as in the flash light of a smartphone or in the display of a television or computer. The basics of a luminescence process is the absorption of energy by the phosphor, followed by emission of a photon typically in the VIS or UV wavelength.¹⁶ The absorbed energy can be electric, mechanic, chemical or electromagnetic radiation in which the latter is called photoluminescence.

These photoluminescence complexes typically exist of a host material that contains a luminescent centre ion called an activator. The role of the activator is to absorb and emit radiation; however, this is not necessarily the case for every phosphor as the role of absorbing the radiation is not restricted to the emitting ion. A sensitizer, be it another dopant or the host lattice could instead absorb and transfer the energy to the activator ion that subsequently emits the energy in the form of light. The energy of the emission is usually lower than the energy of the absorption of the same transition. This is known as the Stokes shift. In rare cases, the opposite can happen in which the energy of the emission is higher than that of the absorption, this is known as anti-Stokes emission. Usually, host lattices with close lattice matches with Lanthanides do not have a big influence on the luminescent properties as these are optically inactive in the lower energy regime (UV ~ IR), its main role is to contain the dopant-ions. In addition, it is important to choose a host material with low phonon energy to minimize non-radiative relaxation and a host with good chemical and thermal stability.^{13, 16}

In general, luminescence is not a simple process, many mechanisms can be involved in luminescence including processes wherein no radiative emission is produced. Instead, the absorbed energy dissipates as heat in the lattice in a so-called non-radiative decay process. While great advances have already been made, a substantial amount of research is still being done as of today.

2.2 Lanthanides

One category of phosphors are lanthanide-doped phosphors. Lanthanides (Ln) are a group of elements listed in the second last row of the bottom of the periodic table. The group starts with Lanthanum with atomic number 57 and ends at Lutetium with atomic number 71. This group is known by another commonly used term, the rare earths (RE) which includes Yttrium and Scandium since their chemical properties are similar to the Lanthanides.

When Lanthanides are incorporated into a solid, they most commonly substitute in the trivalent (Ln^{3+}) ionic state resulting in the $[\text{Xe}] 4f^n$ ground state in which n is the number of electrons ranging from 0 – 14. The Ln^{3+} ions are known to experience lanthanide contraction which means that the ionic radius decreases across the series. This is due to the poor shielding of the increasing positive charge of the nucleus from the 4f electrons as visualized in Figure 2.1.¹⁷

It is important to realize that the trivalent lanthanide ions have filled $5s^2$ and $5p^6$ shells that are further away from the nucleus and to some extent shields the 4f electrons from external influences. Due to this shielding, the trivalent Ln^{3+} ions behave optically like free ions. This causes the Lanthanides to have sharp absorption, emission lines and weak coupling with lattice vibrations arising from the partly filled and shielded 4f orbitals. These sharp emission lines and weak crystal field influences makes the Lanthanides interesting and ideal for photoluminescent materials.¹⁶

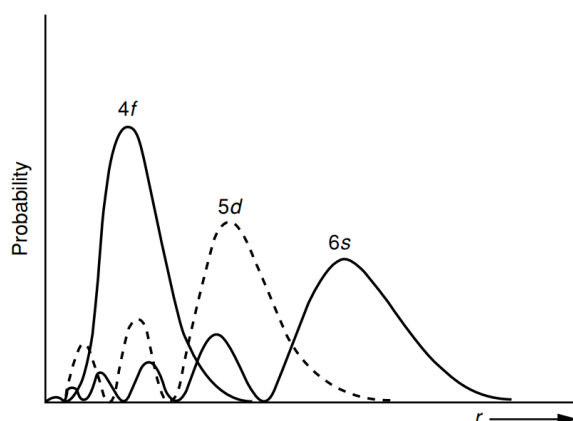


Figure 2.1: Plot of the wavefunctions for the lanthanide orbitals. The probability to find an electron at a distance r is plotted.

The origins of the unique optical properties and energy levels of the Lanthanides are caused by Coulomb interactions between $4f^n$ electrons, spin-orbit coupling and crystal-field splitting, resulting in a rich energy level structure for the 4f states. These states are recorded in the Dieke diagram in Figure 2.2 for each of the various trivalent Lanthanides. The width of the bars indicate the order of magnitude for the crystal field splitting which are dependent on the host lattice but small in general.¹⁸ The $4f^n$ - $4f^n$ transitions within the elements are Laporte forbidden by the quantum mechanical selection rules.¹⁹ The parity forbidden characteristic results in typically small probability of $4f^n$ - $4f^n$ transitions, but it is slightly lifted by the opposite parity mixing of for example 5d wave functions into the 4f wave functions. This leads to the transitions having typically long-living excited states ($\sim 10^{-3}$ s).

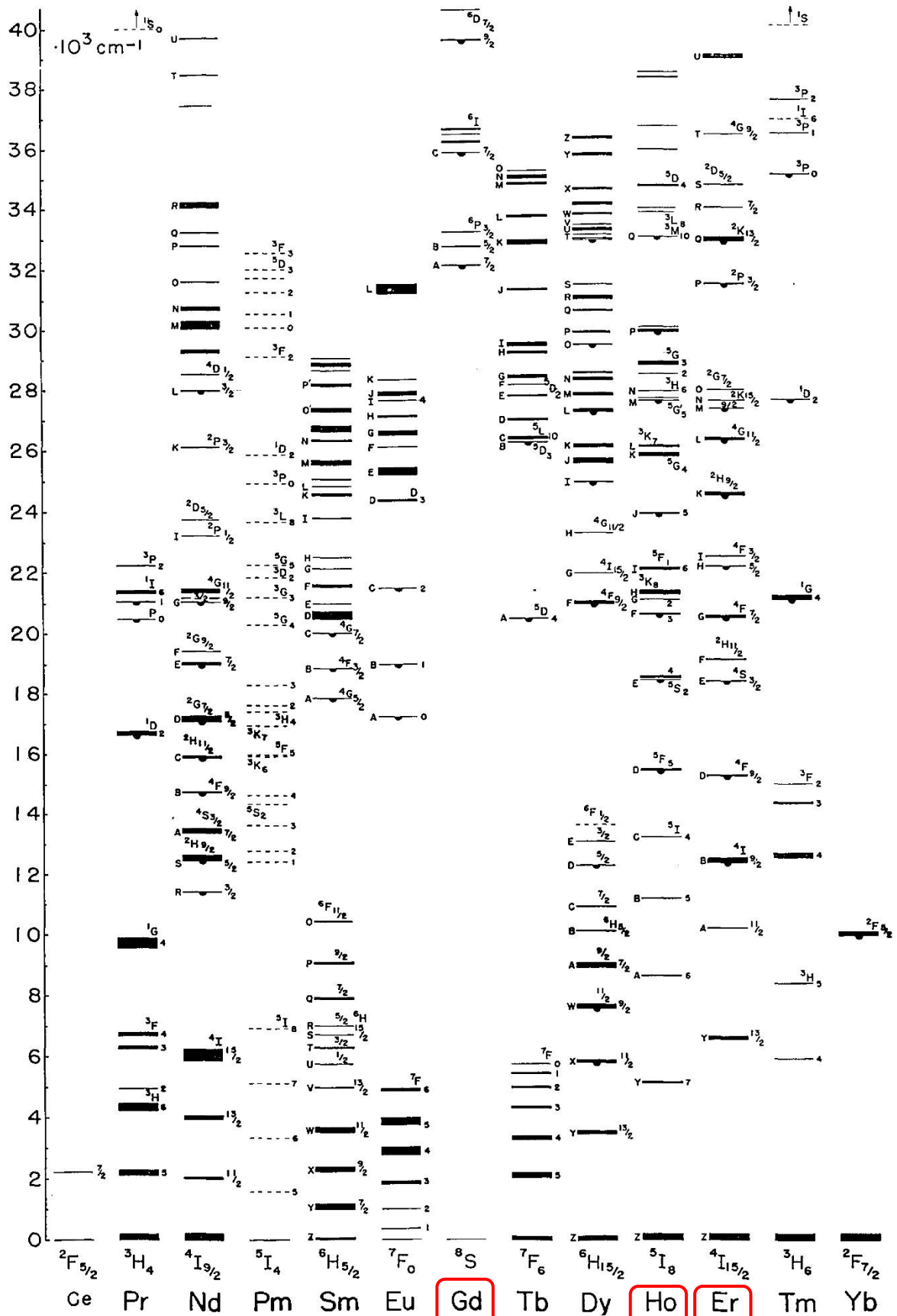


Figure 2.2: The Dieke diagram showing the energy level structure of the lanthanide ions arising from interactions in the inner $4f^n$ shell.

4fⁿ states of Lanthanides

The 4fⁿ energy levels or states originate from (in decreasing order of magnitude) Coulomb interactions between 4fⁿ electrons (mutual repulsions of electrons), spin-orbit coupling (coupling between spin and orbital angular momentum) and crystal-field splitting as illustrated in Figure 2.3. Electronic structures of atoms are typically given by their electronic configurations. This however misses a big part which is the arrangement of the electrons in the atoms. These different occupation configurations are called microstates which have their basic set of notation rules. To explain this notation, a set of quantum numbers originating from Schrödinger's wave equations are needed:

- Principal (n) = 1, 2, 3.. (describes the size of the orbital e.g. the "1" in 1s or the "5" in 5d orbitals.)
- Angular (l) = 0, 1, 2, 3.. (describes the shape of the orbitals and corresponds to the s, p, d, f... orbitals)
- Magnetic (m_l) = $-l \leq m_l \leq +l$ (describes the orientation in space of an orbital)
- Spin orientation (m_s) = $\pm \frac{1}{2}$ (intrinsic property of electrons)

Collectively, they can be arranged into what is called a term symbol expressed as ^{2S+1}L in which S is the total spin ($S = \sum_i m_s$), $2S+1$ is the spin multiplicity and L is the total orbital angular momentum ($L = \sum_i m_l$). When the spin and orbital angular momenta of individual electrons are strongly coupled, the spin-orbit coupling (J) is added which results in the term symbol expressed as $^{2S+1}L_J$. The value of J ranges from $L - S \leq J \leq L + S$. To find the term with the lowest energy, Hund's rules are applied in which first S is maximized followed by L and then depending on if the shell is less than or half-filled or more, the ground term for J is respectively the lowest value or the highest value.²⁰ As an example, to find the ground state of Ho^{3+} we know that the electronic configuration is $4f^{10}$ which corresponds to $S=2$, $L=6$ and J ranges from 4~8. This corresponds to the term symbol 5I_J in which $J=8$ is the ground state. General selection rules for the 4fⁿ-4fⁿ transitions in Lanthanides are given in Table 2.1.²¹

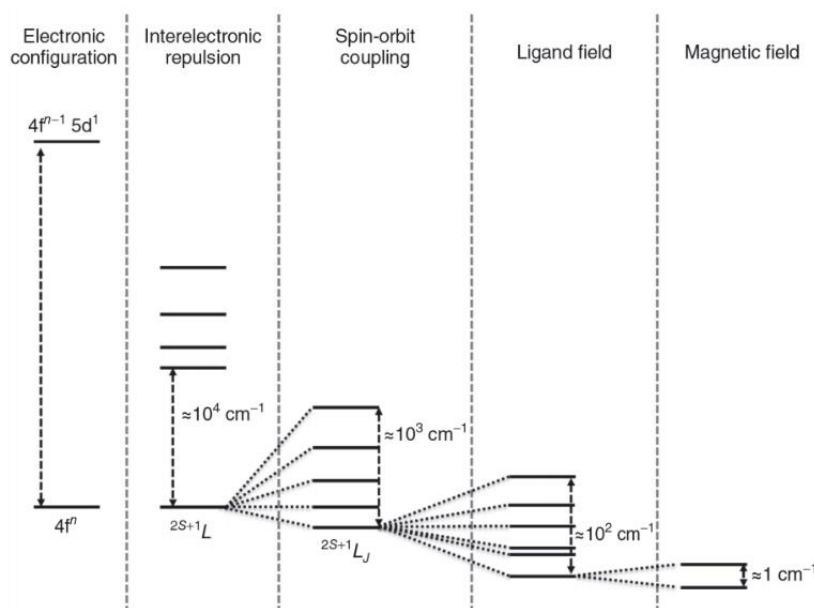


Figure 2.3: A schematic overview of the order of magnitude and the way that the energy levels of the Lanthanides are split.

Transition type	S L J selection rules (Forbidden transitions)	Order of magnitude of oscillator strength
Electric Dipole (ED)	$\Delta S=0; \Delta L \leq 1 (0 \leftrightarrow 0); \Delta J \leq 1 (0 \leftrightarrow 0)$	$\sim 0.01-1$
Forced ED	$\Delta S=0; \Delta L \leq 6 (L \text{ or } L'=0; 0 \leftrightarrow 0); \Delta L =2,4,6; \Delta J \leq 6 (J \text{ or } J'=0; 0 \leftrightarrow 0); \Delta J =2,4,6.$	$\sim 10^{-4}$ of ED
Magnetic Dipole (MD)	$\Delta S=0; \Delta L=0; \Delta J \leq 1 (0 \leftrightarrow 0)$	$\sim 10^{-6}$ of ED
Electric quadrupole (EQ)	$\Delta S=0; \Delta L \leq 2 (0 \leftrightarrow 0,1); \Delta J \leq 2 (0 \leftrightarrow 0,1)$	$\sim 10^{-10}$ of ED
One phonon ED vibronic	Same as Forced ED	$\sim 10^{-6}$ of ED

Table 2.1: A summary of the SLJ selection rules for electronic transitions of trivalent-lanthanide ions.

2.3 Upconversion

There are four classes of UC mechanisms which are based on the absorption of two or more photons via metastable and long-lived intermediate states that leads to population of a higher excited state from which emission occurs.²² These four UC mechanisms are schematically illustrated in Figure 2.4 which are; Excited State Absorption (ESA), Energy-Transfer Upconversion (ETU), Cooperative sensitization and Photon Avalanche (PA). The illustration includes the conventional photoluminescence scheme (a.) this depicts absorption of energy (such as a photon or other energy transfer process) which promotes the ion to the second excited state. In turn, the excited state is relaxed towards the emitting state by nonradiative vibrational relaxation and subsequently falls back to the ground state while emitting a lower energy photon.

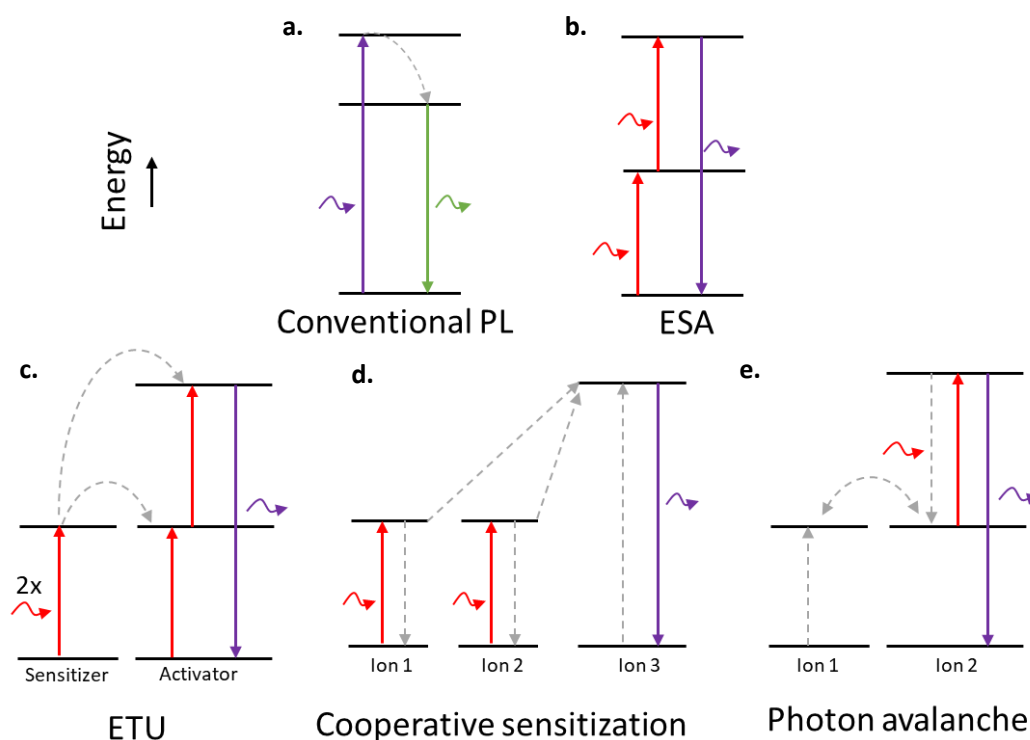


Figure 2.4: Schematic diagrams for upconversion mechanisms: **a.** Conventional photoluminescence. **b.** Excited State Absorption. **c.** Energy Transfer Upconversion **d.** Cooperative sensitization **e.** Photon Avalanche.

Upconversion emission are anti-Stokes processes which works as depicted in Figure 2.4: **b.** ESA is a single ion process that requires the absorption of two photons which promotes the electron to the second excited energy state with the subsequent emission from the second excited state towards the ground state. **c.** In the ETU process, the sensitizer absorbs and transfers two or more photons to the nearest activator followed by emission from the activator. **d.** In cooperative sensitization, two ions are required to simultaneously transfer their energy to a higher state of the activator ion. **e.** PA is more complex than the previous mechanisms, this process requires a non-resonant ground state absorption (GSA) of a photon which is resonant with an ESA or ETU transition.²³ It should be noted that the UC mechanisms are not only limited to these four possibilities, there can be combinations of these processes for example ET followed by ESA.²⁴ In general, three different classes of UC materials exist which are: rare-earth-doped, triplet-triplet annihilation using organic molecules and quantum nanostructures.²⁵ This thesis will only focus on the rare-earth upconversion materials.

As stated in the introduction, the couples Erbium-Gadolinium ($\text{Er}^{3+}\text{-Gd}^{3+}$) and Holmium-Gadolinium ($\text{Ho}^{3+}\text{-Gd}^{3+}$) were explored in this project. This choice was made using the Dieke diagram in Figure 2.2 in which the investigated Lanthanides are marked. Due to the Gadolinium (Gd^{3+}) having an especially stable $^8\text{S}_{7/2}$ ground state, the excited levels are at high energies starting at 32 000 cm^{-1} . The first excited state of Gd^{3+} is $^6\text{P}_{7/2}$ with a wavelength of roughly 313 nm which means that Gd^{3+} has emission levels in the exact desired UVB wavelength.¹⁶ To obtain the emission by blue-to-UVB upconversion from this state, two conditions must be met. The first one is that the sensitizer needs a long living intermediate state which is excitable with blue (~ 450 nm). And secondly, a state higher than the 313 nm Gd^{3+} state that is excitable by ETU with 450 nm is required for the sensitizer. These conditions are met by Dysprosium, Holmium, Erbium and Thulium. However, in this project we only study the ($\text{Er}^{3+}\text{-Gd}^{3+}$) and ($\text{Ho}^{3+}\text{-Gd}^{3+}$) couples. The possible upconversion mechanisms for these couples are illustrated in Figure 2.5. In Figure 2.5 **a.** The $^2\text{K}_{13/2}$ state of Er^{3+} can be excited by the $^4\text{S}_{3/2}$ by UC via cross-relaxation by another Er^{3+} ion and subsequent rapid relaxation occurs from the higher levels. This is then followed by energy transfer to the $^6\text{P}_{3/2}$ and $^6\text{P}_{5/2}$ levels of Gd^{3+} which results in population of the $^6\text{P}_{7/2}$ excited state and 313 nm emission. In Figure 2.5 **b.** the $^3\text{M}_{10}$ level can be filled via ETU from the $^5\text{F}_3$ and $^5\text{S}_2$ levels of Ho^{3+} after which the $^6\text{P}_{3/2}$ and $^6\text{P}_{5/2}$ of Gd^{3+} are excited by energy transfer resulting in 313 nm emission. In these mechanisms the expected intermediate states for Er^{3+} and Ho^{3+} are $^4\text{S}_{3/2}$ and $^5\text{F}_3 / ^5\text{S}_2$ respectively.

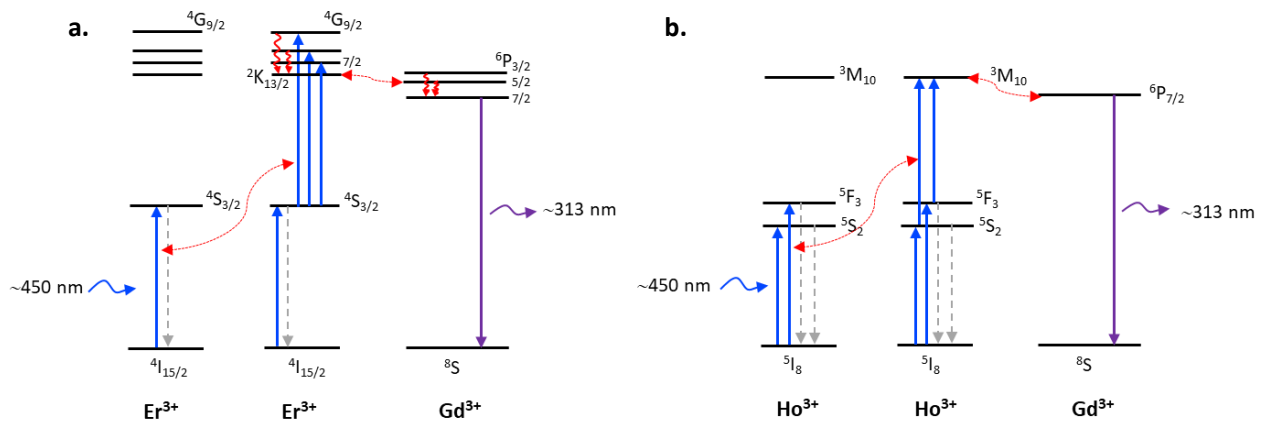


Figure 2.5: Possible upconversion mechanisms for 450 nm blue to UVB upconversion in the **a.** Erbium-Gadolinium and **b.** Holmium-Gadolinium couple.

2.4 Energy Transfer

Energy Transfer (ET) has been mentioned multiple times. ET is an important process in the UC mechanism which becomes more prominent with increasing Ln^{3+} concentrations. ET can be intuitively understood in the following way in which a sensitizer ion absorbs energy and gives its energy to a nearby activator. Different kinds of ET mechanisms exist which can be roughly categorized in two; radiative and non-radiative. In the case of the former, a sensitizer emits a photon which the activator absorbs. In the latter, ET proceeds non-radiatively without emission of a photon.^{16, 13}

Energy transfer is only possible if the energy difference between the ground and excited state of the donor and acceptor are similar (resonance condition) and a suitable interaction between both systems must be present. The interaction can be an exchange interaction (wave function overlap) or an electric or magnetic multipolar interaction. In the case of the resonance condition, the emission band of the donor should spectrally overlap the absorption band of the acceptor. An equation describing the transfer rate was given by Dexter in 1953.²⁶

$$P_{SA} = \frac{2\pi}{\hbar} |\langle S, A^* | H_{SA} | S^*, A \rangle|^2 \times \int g_s(E) g_A(E) dE$$

In this equation, P_{SA} is the transfer rate between sensitizer (S) and activator (A). The integral presents the spectral overlap between S and A and the matrix represents the interaction (in which H_{SA} is the interaction Hamiltonian) between the initial $|S, A^* \rangle$ and final state $|S^*, A \rangle$.

In addition, Förster derived a similar equation for the total energy transfer rate (Γ_{ET})²⁷:

$$\Gamma_{ET} = \frac{2\pi}{\hbar} \frac{\mu_D^2 \mu_A^2 \kappa^2}{r^6 n^4} \int g_s(E) g_A(E) dE$$

In which μ_D and μ_A describe the transition dipole moments of the donor and acceptor, r is the distance between the centre of the dipoles, n is the refractive index of the surrounding medium and the integral again represents the spectral overlap. In this formula the most important thing to notice is the r^{-6} dependency for dipole-dipole transitions. In the case of more dopant ions, the distances of dopant ion to dopant ion will be shorter which increases the chance of dipole-dipole transitions. In addition, increasing the ion concentrations means that the chance of non-radiative relaxation increases via multiple energy transfers (energy migration) towards a quenching agent.

For the tri-valent lanthanide ions, the excited state can dissipate its energy non-radiatively. This can be accompanied by the emission or absorption of lattice phonons (vibrations). Depending on the host lattice, phonon energies can differ. When the phonon energy of a host lattice is high or the energy levels are closely spaced, the energy can be completely lost by multi-phonon relaxation. The multi-phonon relaxation decay rate can be expressed as:

$$W_n = W_0 [1 - \exp\left(-\frac{h\nu}{kT}\right)]^{-\Delta E/h\nu}$$

In which W_n is the rate at temperature T , W_0 is the rate at 0 K, ΔE is the energy gap between the levels and ν is the relevant phonon frequency. When ΔE is equal to or less than 4–5 times the phonon energy, non-radiative multi-phonon relaxation becomes more dominant than the radiative decay.²⁸ In reverse, when the gap to bridge the energy transfer is larger than 5 phonons, no non-radiative relaxation will occur. This means that the concentration of sensitizer and activator ions is preferred to be low and precisely adjusted to avoid the quenching effect.²⁹

Non-radiative recombination can be correlated to the number of defects and impurities in which the excited state is quenched at a defect site or surface state. This is a fast process and leads to quenching of the radiative recombination (emission). In nanoparticles, most of the defects are located at the surface. The atoms in the surface have less neighbours than the atoms inside the bulk which results in dangling bonds. The surface atoms are then unsatisfied which gives rise to strongly localized energy states that are able to trap and quench the excited state.³⁰ The less dopants, the smaller the probability is for energy transfer toward a defect state. Quenching due to many dopant ions is known as concentration quenching.³¹

A few possible pathways for the excited state to transfer its energy have already been mentioned. These are summarized and depicted in Figure 2.6. The first pathway **a.** is the resonant radiative transfer which is the emission of a sensitizer with a subsequent absorption by the activator, second **b.** is the resonant non-radiative transfer which is similar to **a.** but then without emission by the sensitizer, third **c.** is the phonon assisted non-radiative transfer which can happen when there is a mismatch between the energy levels and finally **d.** cross-relaxation is possible when there are more energy levels in between the ground and excited state. In this case there is a possibility of transferring only a part of the energy to the acceptor.³²

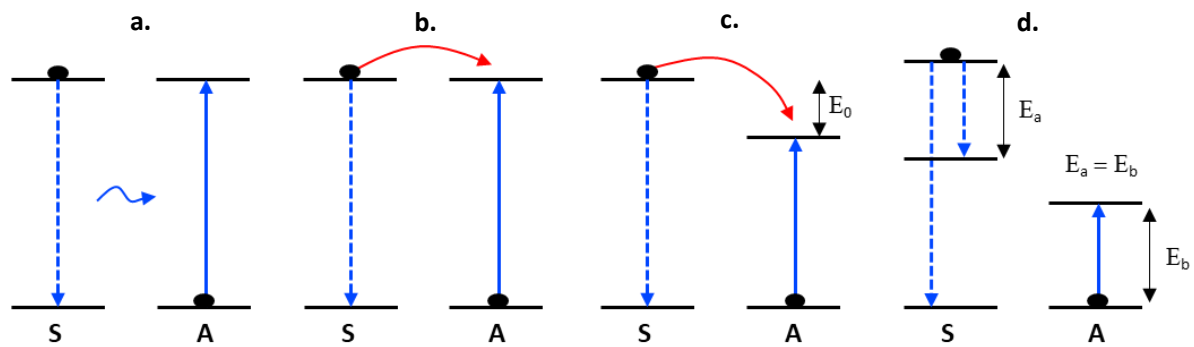


Figure 2.6: Possible energy transfer pathways in a lanthanide co-doped sensitizer (S) and activator (A) system.

2.5 Quenching pathways

Multiple quenching pathways have been addressed which are summarized in this section. First there is the concentration quenching between the individual dopant ions which includes cross-relaxation and energy migration towards a quenching agent. Figure 2.7 **a.** shows how the intermediate states of Er^{3+} and Ho^{3+} ions can quench itself via the concentration quenching pathways and the Gd^{3+} ions can likewise quench themselves due to energy migration.³¹

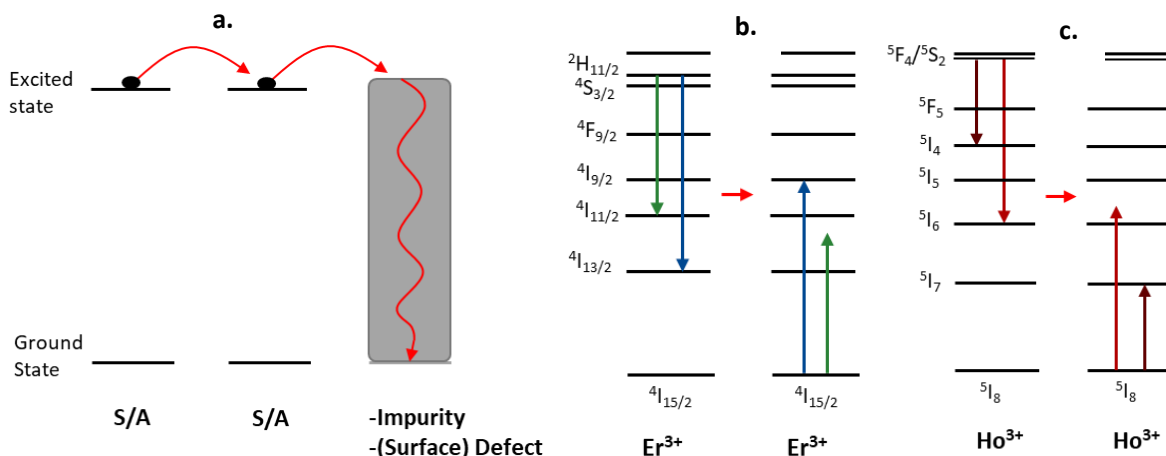


Figure 2.7: Various concentration quenching pathways in the Er^{3+} - Gd^{3+} and Ho^{3+} - Gd^{3+} dopant couples. **a.** depicts the concentration quenching due to energy migration towards a quenching agent. **b.** depicts the cross-relaxation pathways between Er^{3+} ions and in **c.** the cross-relaxation pathways between Ho^{3+} ions.

Figure 2.7 **b.** and **c.** depict cross-relaxation mechanisms in Er^{3+} and in Ho^{3+} ions respectively. In Er^{3+} this occurs between Er^{3+} ions at separations of 1 nm or less where the energy from the $^2\text{H}_{11/2}$ state towards the $^4\text{I}_{11/2}/^4\text{I}_{13/2}$ state is transferred to the ground state of another Er^{3+} ion.³⁰ In Ho^{3+} this could happen in which the energy from the $^5\text{F}_4/^5\text{S}_2$ state to the $^5\text{I}_4/^5\text{I}_6$ states are transferred to the ground state of a neighbouring Ho^{3+} ion.

Another quenching possibility of the 313 nm blue-to-UVB UC peak is the phonon assisted energy back-transfer (BET) between the nearly resonant Gd^{3+} : $^6\text{P}_{7/2}$ and Er^{3+} : $^2\text{P}_{3/2}$ states for the Er^{3+} - Gd^{3+} couple and Ho^{3+} : states in the $30 \times 10^3 \text{ cm}^{-1}$.³³ When less than 5 lattice phonons are needed to overcome the energy gap between the energy back-transfer states it will become a probable occurrence. The lattice phonon energy of cubic Y_2O_3 is approximately $\sim 600 \text{ cm}^{-1}$.³⁴ As can be seen in Figure 2.8, the energy differences of the back-transfer are able to be covered by less than 5 lattice phonons that is: ~ 1 phonon for Er^{3+} and ~ 3.5 phonons for Ho^{3+} .

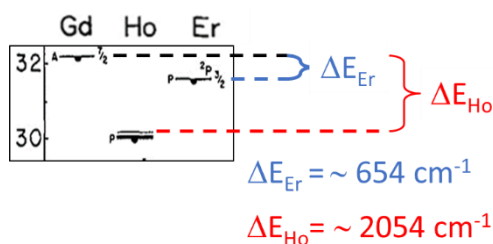


Figure 2.8: Phonon energy difference between the 313 nm emitting state ($^6\text{P}_{7/2}$) of Gd^{3+} and the first lower excited states of Ho^{3+} and Er^{3+} .

2.6 Lifetime of photoluminescence

Various pathways for photoluminescence exist in a phosphor. Using lifetime measurements an average can be calculated for the duration of the excited state before returning to the ground state. The lifetime can give crucial information of for example the frequency of encounters with quenching agents and rate of energy transfer.³⁵ In the pulsed lifetime measurements, an initial population (N_0) is excited. The decay rate of this population is:

$$\frac{dN(t)}{dt} = -(\gamma + k + \varepsilon)N(t)$$

Where $N(t)$ is the number of excited states at time t after the excitation pulse, γ is the emission rate, k is the rate of non-radiative decay and ε is the rate of energy transfer.³⁶ Integration of this equation while keeping in mind that $N(t) = N_0$ at $t = 0$ yields:

$$N(t) = N_0 e^{-t/\tau}$$

In this equation $\tau = (\gamma + k + \varepsilon)^{-1}$ is the lifetime of the excited state. An important point is that when multiple processes such as non-radiative and energy transfer are involved in the excited state relaxation, the decay curve will not follow a single exponential behaviour. Hence, the measured decay curves will follow a multi-exponential behaviour. The average lifetime $\bar{\tau}$ can be calculated by the equation:

$$\bar{\tau} = \frac{\sum_i a_i \tau_i^2}{\sum_i a_i \tau_i}$$

In which a_i and τ_i represent the amplitude and decay time respectively of the individual components for multi-exponential decay profiles.³⁷

3. Experimental

The aim of this work is to find a suitable and efficient lanthanide upconversion couple for blue- (~450 nm) to-UVB (~313 nm). The couples which in theory could work are the Erbium-Gadolinium and the Holmium-Gadolinium couple. To explore them, both microcrystalline Y_2O_3 : %Er, %Gd and Y_2O_3 : %Ho, %Gd samples were synthesized to observe blue-to-UVB UC. After successfully obtaining this, the efficiency was optimized by tuning the concentration of the dopants which gave an indication of the most efficient dopant concentration in nanocrystalline Y_2O_3 particles. The reason that the blue-to-UVB UC was broadly optimized in microcrystalline particles and not in nanocrystalline is that the synthesis is fast and easier. Finally, the synthesis of nanocrystalline Y_2O_3 was required to perform the same analysis and assess the efficiency and influence of particle size of the blue-to-UVB UC.

3.1 Synthesis

To synthesize Lanthanide doped particles, various methods exist depending on the preferred size and shape of the particles. Synthesis of micro-sized (bulk) particles require fewer complicated steps such as ball milling or grinding using an agate mortar and pestle with both a subsequent sintering treatment.³⁸ The method used to synthesize the microcrystalline and nanocrystalline Y_2O_3 particles was by “wet synthesis” in which the prepared precursors are used in solution. The advantages of using wet chemistry synthesis over grinding is the substantial amount of control over the precision in dopant concentration, time-efficiency and a homogeneous distributed mixture.

3.1.1 Microcrystalline Y_2O_3

Stock solutions of known concentrations of $\text{Ln}(\text{NO}_3)_3$ were first prepared in separate volumetric flasks. The rare-earth oxides: Y_2O_3 (99.999% purity) purchased from Alfa Aesar, Er_2O_3 , Ho_2O_3 and Gd_2O_3 purchased from Highways International were dissolved in HNO_3 (65% purity) purchased from Honeywell Fluka and then added together in a beaker in the preferred dopant concentrations under magnetic stirring. After stirring for around 30 min, excess oxalic acid purchased from Baker Analyzed was used to precipitate the rare earth ions. The precipitate was collected by centrifugation and washed three times using DI water. The powders were then dried on a heating plate overnight at ca. 90 °C and finally calcinated in a tube oven for 5 h at 1200 °C (Oven settings: ramp 5°C/min, first dwell for 2 h at $T=500^\circ\text{C}$, ramp 5°C/min until 1200°C, second dwell for 5 h, cool down naturally till ambient temperature).³⁹

3.1.2 Nanocrystalline Y_2O_3

The nanocrystalline particles were synthesized based on the most efficient blue-to-UV UC concentration determined in the microcrystalline particles. It was quickly realised that the NP synthesis was not trivial, for this reason, various methods were tested. After the colloidal syntheses, the resulting NPs were freeze-dried and calcined in various settings.

Method A (RE-Carbonates)

Method A is based on the paper of Hongzhi Wang, *et al.*⁴⁰ in which they succeeded in making Y₂O₃: Eu nanocrystals. Following this method, RE-carbonates (Y₂(CO₃)₃ xH₂O, Ho₂(CO₃)₃ xH₂O and Gd₂(CO₃)₃ xH₂O) purchased from Alfa Aesar (99.9% purity) were first dissolved in Oleic Acid purchased from Sigma-Aldrich (90% purity) overnight at 60°C till clear. The solution was mixed in a three-neck round-bottom flask with oleylamine purchased from Acros Organics (80-90% Purity) and dehydrated under vacuum at 70°C for 1 h with magnetic stirring. The solution was then increased to 230°C for 2 h under N₂ atmosphere. Subsequently, the product was heated to 280°C for 30 min and cooled down naturally to room temperature. After the mixture cooled down, methanol purchased from VWR Chemicals (99.85% purity) was added resulting in a turbid solution. The precipitate was collected by centrifugation and washed using a toluene/methanol solution for three times. Afterwards the precipitate was dispersed in toluene purchased from VWR Chemicals (99.9% purity) for freeze-drying which resulted in a fine white powder.

Method B (RE-Chlorides)

Method B is based on the synthesis method of Yue Pan, *et al.*⁴¹ in which they successfully made Eu²⁺/Eu³⁺ co-doped Sc₂O₃ NPs. RECl₃ hexahydrates (YCl₃ purchased from Acros organics (99.999% purity), HoCl₃ purchased from Sigma-Aldrich (99.9% purity) and GdCl₃ purchased from Strem Chemicals (99.9% purity)) were mixed with 20 mL of oleylamine in a three-neck round-bottom flask which was then heated to 160°C for 30 min with magnetic stirring under N₂ atmosphere. The reaction mixture was then further heated to 310°C for 1 h. Afterwards the reaction mixture was cooled down to room temperature and the products were precipitated by adding ethanol purchased from VWR Chemicals. The resulting Y₂O₃ NPs were collected by centrifugation for 5 min at 8000 rpm, washed with the mixture of cyclohexane purchased from Acros Organics (99.8% Purity) and ethanol for three times, and re-dispersed in cyclohexane for freeze-drying which resulted into a fine white powder.

Method C (RE-Nitrates)

The third and last method, Method C is based off of the homogeneous precipitation method by Seungman Sohn, *et al.*³⁸ They succeeded in the synthesis of near-monodisperse Y₂O₃ particles however, the sizes of the particles are quite large (typically larger than 100 nm). This technique was mainly used to determine the size dependency of the blue-to-UVB UC. In a three-neck round-bottom flask, RE₂(NO₃)₃ (Y₂(NO₃)₃: hexahydrate purchased from Sigma-Aldrich, 99.8% purity, Ho₂(NO₃)₃ Purchased from Alfa Aesar, 99.9% purity and Gd₂(NO₃)₃ purchased from Sigma-Aldrich, 99.99% purity) and Urea purchased from Baker Analyzed were added together with 50 mL DI water. This mixture was stirred with a magnetic stirrer until it was clear, afterwards it was heated to 85°C and kept at this temperature for 2 h. Finally, the solution was left to cool until ambient temperature. The resulting solution was turbid with the Y₂O₃ NPs which were precipitated by centrifugation and washed three times using DI water and ethanol. The water was evaporated by placing it in an oven at 100°C overnight and the resulting powder was calcinated in a tube oven at 800°C for 3h.

3.2 Characterization & Optical Spectroscopy

3.2.1 Crystal structure & Morphology

To determine if the synthesis was successful, structural and spectroscopic measurements were performed. The crystal structure was assessed by powder X-Ray diffraction using a PW 1729 X-ray generator by Philips operating at 40 kV and 20 mA coupled with a Philips PW1820 Automated Powder Diffractometer utilizing Cu K α radiation. The synthesized powders were put into an aluminium sample holder and the diffractograms were scanned from ($2\theta=$) 10 to 80°. The aluminium sample holder peaks could be detected in the diffractograms which should be kept in mind.

Transmission Electron Microscopy (TEM) images were taken with a Tecnai 10 Philips microscope using a Backscattered-electron (BSE) detector. TEM grids were made by first dispersing the powder NPs and then dripping the solution onto the Formvar coated copper TEM-grids.

3.2.2 Optical properties & Upconversion

For the optical properties, photoluminescence (emission and excitation) spectra were obtained by performing spectroscopic measurements using an Edinburgh Instruments FLS920 spectrofluorometer coupled with a 450W xenon lamp as excitation source and Hamamatsu R928 photomultiplier tube detector.

For upconversion, xenon lamps are not strong enough to result in good measurements. For this reason, a pulsed laser was used to do blue-to-UVB UC measurements. Pulsed lasers can deliver light with more intensity. The optical power appears in pulses of some duration at some repetition rate. The pulse energy is equal to the average power divided by the repetition rate. It is possible to lower the rate of pulses so that more energy is build up in between pulses. The utilized pulsed laser was a color-tunable Opotek HE 355II laser (20 Hz and ~10 ns pulses). The lifetime of the upconversion emission were recorded by using the Edinburgh Instruments FLS920 and the Opotek laser. Every measurement using the Opotek laser was performed by using 100% power output.

A continuous-wave laser (CW-laser) was used to approximate the upconversion intensity using a blue light LED source. The CW-laser delivers light of less intensity than the pulsed Opotek. A ~450 nm Blue Dot Laser by Laserlands (2.5W) was used. However, the laser was not of good quality which created too much noise in the spectra to be included in the main results. The results of the CW-laser measurements can be found in Appendix A.

4. Results & Discussion

4.1 Microcrystalline Y_2O_3 : Er /Ho, Gd

Several samples with different concentrations of the dopants Er^{3+} - Gd^{3+} and Ho^{3+} - Gd^{3+} have been made to optimize the blue-to-UV upconversion (UV-UC). At first, 12 samples for both couples were made. The exact concentrations are tabulated in Table 4.1. These concentrations were further optimized in a small concentration range above and below the initial most efficient concentrations for Blue-to-UV UC (see Table 4.2).

$Y_{2(1-x-y)}Ho_xGd_yO_3$ Samples	Ho (%)	Gd (%)	$Y_{2(1-x-y)}Er_xGd_yO_3$ Samples	Er (%)	Gd (%)
1	0.5	0	13	1	0
2	0.5	10	14	1	10
3	0.5	25	15	1	25
4	0.5	99.5	16	1	99
5	1	0	17	3	0
6	1	10	18	3	10
7	1	25	19	3	25
8	1	99	20	3	97
9	3	0	21	7	0
10	3	10	22	7	10
11	3	25	23	7	25
12	3	97	24	7	93

Table 4.1: The dopant concentrations of the initial exploration of microcrystalline Y_2O_3 samples with the Ho^{3+} - Gd^{3+} and Er^{3+} - Gd^{3+} dopant couples to examine the range for the most efficient blue-to-UVB UC concentration.

Optimization [Ho^{3+}] Samples	Ho (%)	Gd (%)	Optimization [Er^{3+}] Samples	Er (%)	Gd (%)
25	0.3	3	32	1	5
26	0.3	10	33	1	2.5
27	0.5	5			
28	0.5	7.5			
29	0.5	12.5			
30	0.5	15			
31	0.7	10			

Table 4.2: Dopant concentrations used for the optimization of microcrystalline Y_2O_3 samples with the Ho^{3+} - Gd^{3+} and Er^{3+} - Gd^{3+} dopant couples for blue-to-UVB UC.

4.1.1 XRD Results

To investigate the phase purity of the Ln^{3+} -doped Y_2O_3 powders, XRD diffractograms were obtained. These results are shown in Figure 4.1 with the red dotted lines as guides for the strongest diffraction peaks of the phase pure Y_2O_3 and Gd_2O_3 reference. For the Er^{3+} - Gd^{3+} couple, the sample with the lowest dopant concentration matches well with phase pure Y_2O_3 . As the dopant concentration increases (1% Er \rightarrow 7% Er, 0% Gd \rightarrow 93% Gd) there is a slight shift in the peak positions towards the right and then back to the left. This shifting is probably due to the deformation of the Y_2O_3 lattice as more dopants with different radii enter (the ionic radii of the RE for the octahedral geometry are: $\text{Y}^{3+} = 90$ pm, $\text{Gd}^{3+} = 94$ pm, $\text{Er}^{3+} = 89$ pm and $\text{Ho}^{3+} = 90$ pm).²⁰ Likewise in the diffractograms of the Ho^{3+} - Gd^{3+} doped Y_2O_3 the peaks align fully in the lower dopant concentrations with a shift towards the left as the concentrations increase (0.5% Ho \rightarrow 3% Ho, 0% Gd \rightarrow 97% Gd).

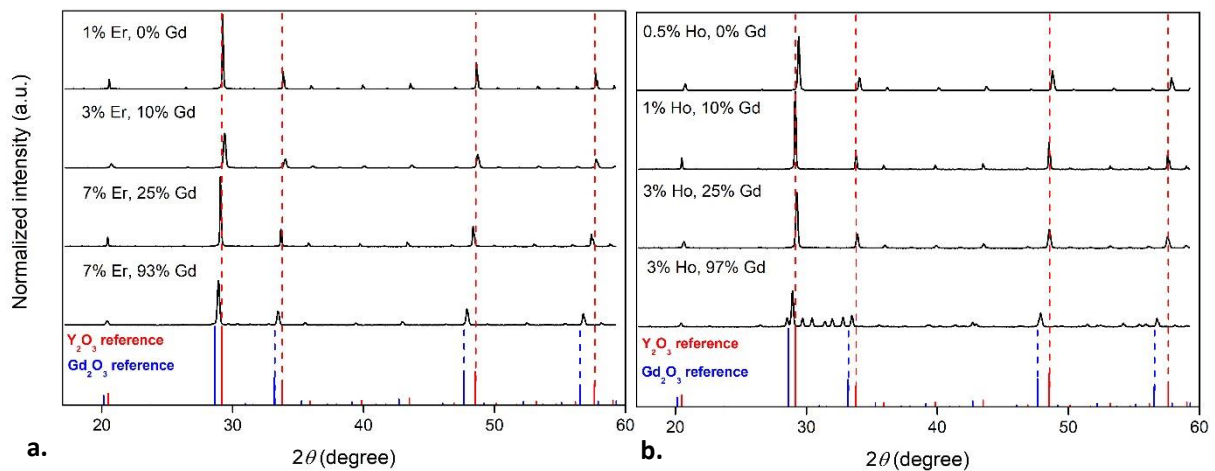


Figure 4.1: XRD spectra of selected microcrystalline **a.** Y_2O_3 : x% Ho, y% Gd and **b.** Y_2O_3 : x% Er, y% Gd samples including phase pure reference diffractograms in red for the Y_2O_3 and in blue for Gd_2O_3 .

It is apparent that the samples with no Y^{3+} ions (7% Er, 93% Gd and 3% Ho, 97% Gd) have a similar structure to the phase pure Y_2O_3 shifted to the left. This is due to the similar crystal structure of Gd_2O_3 with Y_2O_3 . There are some peaks that do not fully align, mainly the many smaller peaks in the 28–34° range in the 3% Ho, 97% Gd sample. These should be features coming from the Gd_2O_3 and Ho_2O_3 crystalline phases.

As shown in the diffractograms of Figure 4.1, the peaks can shift due to increase in dopant concentrations. The calcination temperature and the duration can play a role. To rule out the possibility of impurities or defects in the crystal lattice, the samples were recalcined at higher temperature for a short duration at 1500°C for 2 h (settings: ramp 5°C/min until 1250°C then ramp 2°C/min until 1500°C, dwell for 2 h, cool down naturally to ambient temperature). If there would be a change in the crystal lattice, it would indicate that at higher temperature the lattice defects can be annealed, meaning that there were still some defects or impurities left after the first calcination treatment.

As we can observe in Figure 4.2, the second calcination does not result in significant changes in the crystalline phase. Only a small change is observed in the samples without Y^{3+} ions. It seems that in the 7% Er, 93% Gd sample, the smaller peaks are more prevalent after calcination at higher temperature. In the 3% Ho, 97% Gd sample we observe similar changes. This can indicate a more phase pure Gd_2O_3 lattice formation.

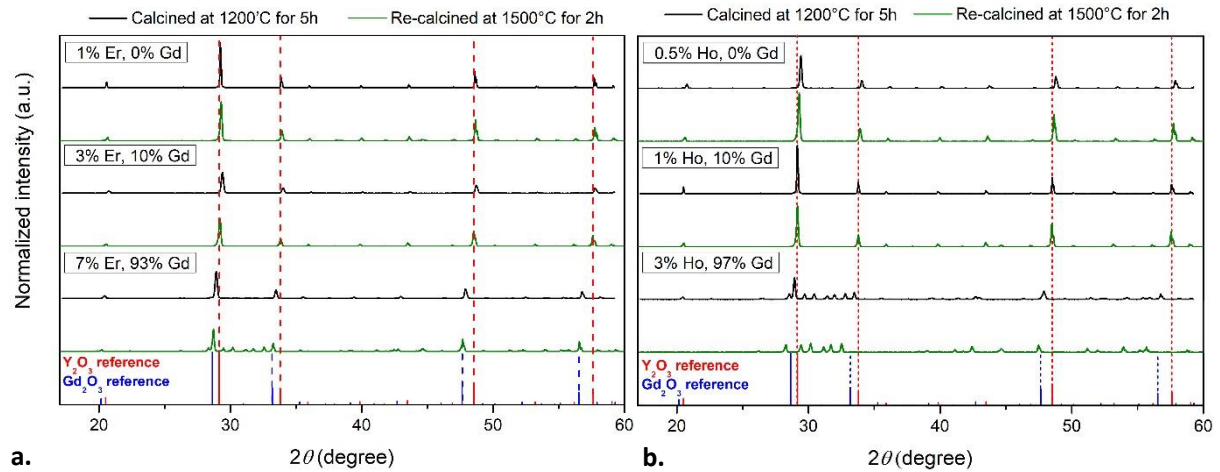


Figure 4.2: XRD spectra of selected microcrystalline **a.** Y_2O_3 : x% Ho, y% Gd and **b.** Y_2O_3 : x% Er, y% Gd samples measured after one (black) and two calcination treatments (green) including a reference diffractogram for the phase pure Y_2O_3 (red) and Gd_2O_3 (blue).

As a conclusion, it can be confirmed that the calcination temperature at 1200°C for 5 h is enough to form the phase pure Y_2O_3 lattice for the samples with small concentration of dopants. Nevertheless, calcination at higher temperature may influence the optical properties which will be addressed in the next chapter.

4.1.2 Photoluminescence results

To assess whether the synthesized powders have the characteristic dopant (Ho^{3+} and Er^{3+}) excitation and emission states, photoluminescence (PL) emission and excitation measurements were performed. Moreover, this serves to determine the exact location (wavelength) of the intermediate state and helps to find out which excitation wavelength around the blue ~ 450 nm results in the optimal intermediate state occupation for blue-to-UVB UC. Finally, blue-to-UVB UC measurements were conducted to determine which concentration of the dopants result in the most efficient upconversion. The observed peaks in the PL graphs are assigned to the electronic transitions of Ho^{3+} , Er^{3+} and Gd^{3+} according to Dieke's energy level diagram (Figure 2.2).

PL of Erbium-Gadolinium doped Y_2O_3

To investigate the optical properties of the Er^{3+} - Gd^{3+} couple, spectroscopic measurements were performed under identical conditions for the synthesized samples. In Figure 4.3, the excitation and emission spectra of Y_2O_3 : 1% Er^{3+} , y% Gd^{3+} samples are plotted. In the excitation spectra in Figure 4.3 a. plotted from 350 nm to 530 nm while measuring the intensity at 563 nm, every observed excitation peak can be assigned to the f^n-f^n transitions of Er^{3+} using the Dieke diagram. The peaks are listed in Table.4.3. In the lower wavelengths at 312 nm a tiny peak is observed only in the samples including Gd^{3+} ions. We can also notice that when the Gd^{3+} dopant concentration increases, a consequent decrease of the peak intensities is detected. This should be due to the shifting of the excitation peaks towards other wavelengths because the Gd_2O_3 lattice will have different influence on the energy levels resulting in a different amount of splitting. Furthermore, the excitation graph reveals which excitation wavelengths result in population of this $^4\text{S}_{3/2}$ intermediate state. From analysis of these peaks, the ones that are the most interesting are the 453 and 489 nm excitation peaks as these lie the closest to the favoured 450 nm blue light excitation wavelength. Overall this spectrum is in good agreement with the expected 4f excitation states from the Er^{3+} ion. The small 312 nm excitation peak should be the result of Energy transfer from the $^6\text{P}_{5/2}/^6\text{P}_{7/2}$ states of Gd^{3+} towards Er^{3+} and the excitation of the $^2\text{P}_{3/2}$ state of Er^{3+} .

λ_{ex} peaks (nm)	Transitions (Er^{3+})
378	$^4\text{I}_{15/2} \rightarrow ^4\text{G}_{11/2}$
407	$^4\text{I}_{15/2} \rightarrow ^2\text{H}_{9/2}$
453	$^4\text{I}_{15/2} \rightarrow ^4\text{F}_{5/2}$
489	$^4\text{I}_{15/2} \rightarrow ^4\text{F}_{7/2}$
521	$^4\text{I}_{15/2} \rightarrow ^2\text{H}_{11/2}$
536	$^4\text{I}_{15/2} \rightarrow ^4\text{S}_{3/2}$

Table.4.3: Location of the excitation peaks of Er^{3+} - Gd^{3+} doped Y_2O_3 samples and their respective transitions while measuring the $^4\text{S}_{3/2}$ (563 nm) emission.

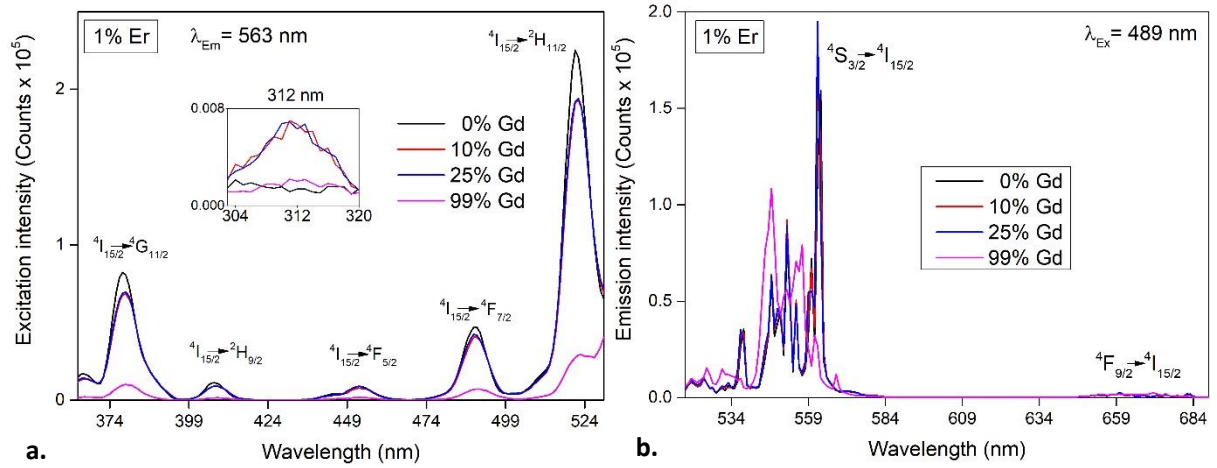


Figure 4.3: PL measurements of $\text{Y}_2\text{O}_3: 1\% \text{ Er}, y\% \text{ Gd}$ (with $y = 0, 10, 25, 99\%$) **a.** Excitation ($\lambda_{\text{Em}} = 563 \text{ nm}$) and **b.** Emission ($\lambda_{\text{Ex}} = 489 \text{ nm}$).

In the emission spectrum (Figure 4.3 **b.**) a cluster of sharp emission peaks from Er^{3+} is located between 529 and 569 nm which arises from the $^2\text{H}_{11/2}$ and $^4\text{S}_{3/2} \rightarrow ^4\text{I}_{15/2}$ transition. There is a very small cluster of peaks located around 660 nm arising from the $^4\text{F}_{9/2} \rightarrow ^4\text{I}_{15/2}$ transition. From this result, it is apparent that the $^4\text{S}_{3/2}$ (563 nm) emission peak is a useful excited state intermediate for blue-to-UV UC because it has the strongest emission intensity. The $^4\text{S}_{3/2}$ emission decreases in the order of $25 > 10 > 0 > 99\% \text{ Gd}^{3+}$. The increase of this peak intensity from 10 to 25% Gd^{3+} could be due to the concentration quenching of Er^{3+} ions being relaxed by the introduction of Gd^{3+} ions. More Gd^{3+} ions will separate the individual Er^{3+} ions resulting in less energy migration between Er^{3+} ions towards a quenching agent. At 99% Gd^{3+} the Y_2O_3 host is completely replaced by Gd_2O_3 and causes the Er^{3+} emission peak maximum to shift towards other wavelengths.

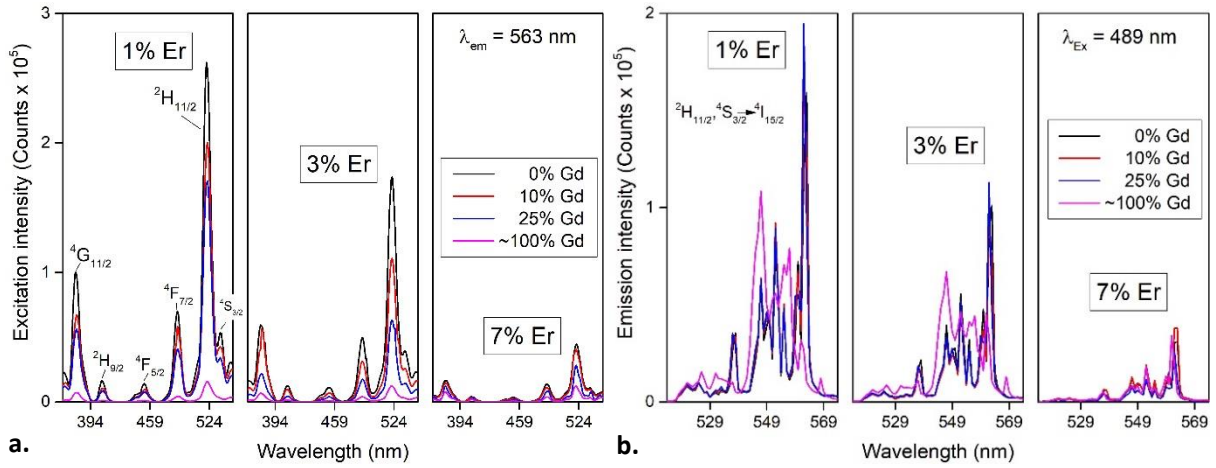


Figure 4.4: PL measurements of Y_2O_3 : 1,3 and 7% Er, y% Gd (with $y = 0, 10, 25, 99\%$) in **a.** Excitation ($\lambda_{em} = 563$ nm) and **b.** Emission ($\lambda_{ex} = 489$ nm).

PL of other concentrations of the Er^{3+} - Gd^{3+} couple were investigated to assess their optical influence. In Figure 4.4, the excitation spectra of 1, 3 and 7% Er^{3+} are plotted next to each other for comparison for both the excitation (**a.**) and emission (**b.**) measurements. Within the Er^{3+} concentrations, the Gd^{3+} concentration is varied with 0, 10, 25 and ~99% Gd^{3+} . The decreasing trend of the excitation intensity in Figure 4.4 **a.** due to increasing concentrations of Er^{3+} and Gd^{3+} can be observed. The highest excitation intensity is found in the 1% Er^{3+} samples.

To assess the concentration dependency of the intermediate state occupation, emission measurements were performed which are plotted in Figure 4.4 **b.** The emission exhibits the same trend as the excitation where the emission intensity (excited with 489 nm) decreases with increasing Er^{3+} . This is most apparent at the 521 nm ($^4S_{3/2}$) peak with the highest intensity at the 1% Er concentration. Therefore, the concentrations of the sensitizer-activator couple for most efficient occupation of the intermediate state $^4S_{3/2}$ was determined to be around 1% for Er^{3+} and 10% for Gd^{3+} . When the concentration of the dopants increases, concentration quenching starts to play a dominant role which suppresses the excitation and emission of the $^4S_{3/2}$ intermediate state. The concentration quenching mechanisms includes cross-relaxation and energy migration towards a quenching agent. Cross-relaxation or self-quenching (Figure 2.6 **b.**) is accounted for the significant decrease of emission intensity with increasing Er^{3+} concentration. This occurs between Er^{3+} ions at separations of 1 nm or less where the energy from the $^2H_{11/2}$ state towards the $^4I_{11/2}/^4I_{13/2}$ state is transferred to the ground state of another Er^{3+} ion.³⁰

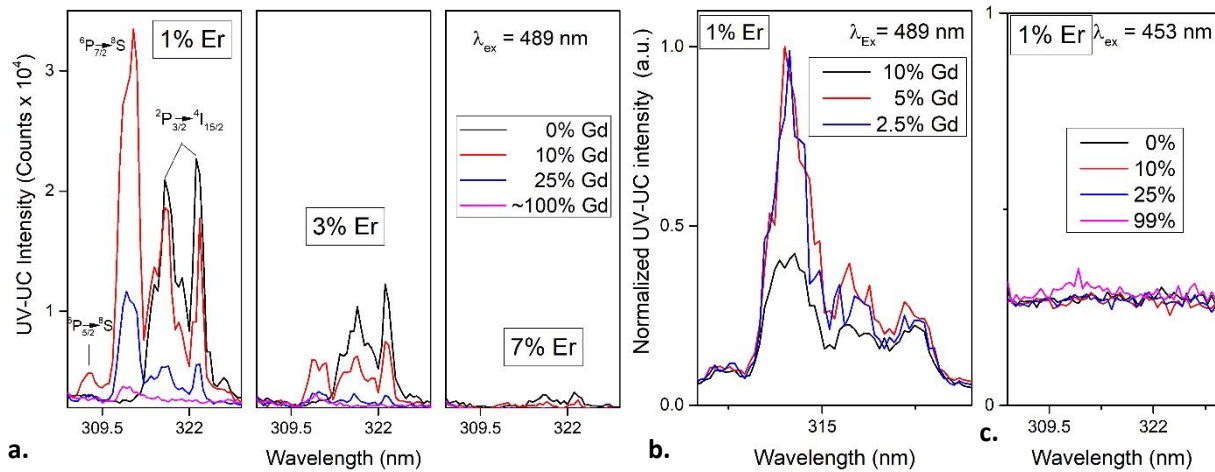


Figure 4.5: **a.**, **b.** Blue-to-UVB UC graphs of the $\text{Y}_2\text{O}_3: x\% \text{Er}^{3+}, y\% \text{Gd}^{3+}$ samples with ($\lambda_{\text{ex}} = 489 \text{ nm}$) and **c.** Blue-to-UVB UC using ($\lambda_{\text{ex}} = 453 \text{ nm}$).

To investigate if the dopant couple exhibit blue-to-UVB UC and to investigate the influence of different concentrations, blue-to-UVB UC measurements were performed while scanning the 260–330 nm region. The Er^{3+} samples were excited by the pulsed Oportek laser using the previously determined effective excitation wavelengths (489 nm and 453 nm). The resulting graphs are plotted in Figure 4.5.

In Figure 4.5 **a.** the plots are ordered with increasing concentration of Er^{3+} next to each other and in every Er^{3+} concentration, the Gd^{3+} concentration was varied (0, 10, 25 and ~99% Gd^{3+}). The blue-to-UVB UC results in several narrow peaks in the 305–325 nm range. These peaks correspond to the emitting states of Gd^{3+} : $^6\text{P}_{5/2} \rightarrow ^8\text{S}$ (307 nm), $^6\text{P}_{7/2} \rightarrow ^8\text{S}$ (313 nm) and Er^{3+} : $^2\text{P}_{3/2} \rightarrow ^4\text{I}_{15/2}$ (319, 323 nm). The small peak at 307 nm is assigned to Gd^{3+} since it does not appear in the graph of the sample without Gd^{3+} (0% Gd^{3+}). The 0% Gd^{3+} sample does not contain Gd^{3+} emitting states which means that the peaks around 322 nm are from the $^2\text{P}_{3/2}$ Er^{3+} state. The concentration of 1% Er^{3+} -10% Gd^{3+} results in the highest upconversion intensity of the 313 nm peak. This is followed by the concentration of 25% Gd^{3+} which indicates concentration quenching due to increasing Gd^{3+} ions. The sample of 99% Gd^{3+} is significantly more quenched. The 313 nm peak shows that successful blue-to-UVB UC is obtained in the samples doped with both Er^{3+} and Gd^{3+} .

To optimize the Blue-to-UVB UC efficiency, Gd^{3+} concentrations were reduced. In Figure 4.5 **b.** the blue-to-UVB UC with concentrations of 10, 5 and 2.5% Gd^{3+} (1% Er) are plotted. The lower Gd^{3+} concentrations (5 and 2.5% Gd^{3+}) exhibits more than twice of the Blue-to-UVB UC intensity of the 10% Gd^{3+} sample. The intensity of this 313 nm peak is similar for both 2.5 and 5% Gd^{3+} . The two $^2\text{P}_{3/2}$ peaks previously assigned to Er^{3+} (319, 323 nm) shows a notably small intensity increase relative to the 313 nm Gd^{3+} peak. Phonon assisted Back Energy Transfer (BET) from the 313 nm emitting $^6\text{P}_{7/2}$ state from Gd^{3+} to the $^2\text{P}_{3/2}$ state of Er^{3+} could contribute to these $^2\text{P}_{3/2}$ peaks (Figure 2.8). Consequently, when the Gd^{3+} concentration decreases, BET will decrease. It can be concluded that the optimal concentration for Gd^{3+} can be approximated to be in the range of 2.5%–5% (1% Er^{3+}).

Blue-to-UVB UC efficiency using the 453 nm excitation was investigated as it is close to the desired 450 nm wavelength. This resulted in the graph in Figure 4.5 c. The graphs do not show the 313 nm emission peak. Only in the 99% Gd³⁺ sample there is a slight signal at the exact 313 nm wavelength. Conclusively, the 453 nm excitation wavelength is inefficient for the Er³⁺-Gd³⁺ couple for blue-to-UVB UC. This was predicted by the low 453 nm excitation intensity of the ⁴S_{3/2} intermediate state of Er³⁺ in the excitation spectrum in Figure 4.4 a.

Microcrystalline Y₂O₃ doped with the Er³⁺-Gd³⁺ couple were successfully synthesized with various dopant concentrations. This was proven by the assessment of the morphology (XRD) and photoluminescence (excitation and emission) in Figure 4.1 and Figure 4.3 respectively. Blue-to-UVB UC was successfully observed (Figure 4.5) and the dopant concentration for the highest blue-to-UVB UC intensity was found to be 1% Er³⁺ with 2.5/5% Gd³⁺. Cross-relaxation and BET were found to be strong quenching mechanisms of the 313 nm UC emission intensity in Er³⁺-Gd³⁺ doped Y₂O₃. A summary of the results can be found in Table 4.4.

Dopants in Y ₂ O ₃	Er ³⁺ & Gd ³⁺
Intermediate state level	⁴ S _{3/2} (563 nm)
Most efficient λ_{Ex}	489 nm
Most efficient UC Concentration	Y ₂ O ₃ : 1% Er ³⁺ , 2.5~5% Gd ³⁺

Table 4.4: Summarized results of the explored microcrystalline Er³⁺-Gd³⁺ doped Y₂O₃.

PL of Holmium-Gadolinium doped Y_2O_3

The optical properties of the Ho^{3+} - Gd^{3+} dopant couple in Y_2O_3 were investigated. This resulted in the excitation and emission spectra in Figure 4.6. Comparative to the Er^{3+} - Gd^{3+} PL results, every excitation peak is assignable to the f^n - f^n transitions of the sensitizer or activator states. In the order of increasing wavelengths, two small peaks at 309 and 313 nm were detected which belongs to the 4f states of Gd^{3+} . The other peaks can be assigned to the Ho^{3+} f^n - f^n transitions which are summarized in Table 4.5. In this spectrum, a very strong signal of the $^5\text{F}_4$ and $^5\text{S}_2$ (~548 nm) intermediate state appears when excited with 448 nm. The intensity of this $^5\text{F}_4$ and $^5\text{S}_2$ intermediate state decreases as the Gd^{3+} dopant increases, the shifting of the peak maxima appears in the 99.5% Gd^{3+} sample like in the Er^{3+} - Gd^{3+} results. The small peaks at 309 and 313 nm are enlarged in Figure 4.6 a. this reveals that their intensities do not follow the same trend as the other peaks ($0 > 10 > 25\% \text{Gd}^{3+}$). Instead they are ordered as $10 > 25 > 99.5 > 0\% \text{Gd}^{3+}$.

λ_{Ex} peaks (nm)	Transitions (Ho^{3+})
335	$^5\text{I}_8 \rightarrow ^6\text{P}_{7/2}$
360	$^5\text{I}_8 \rightarrow ^3\text{H}_6, ^3\text{D}_2$
382	$^5\text{I}_8 \rightarrow ^3\text{G}_4, ^3\text{K}_7$
414	$^5\text{I}_8 \rightarrow ^5\text{G}_5$
448	$^5\text{I}_8 \rightarrow ^5\text{G}_6$
462	$^5\text{I}_8 \rightarrow ^5\text{F}_2, ^3\text{K}_8$
482	$^5\text{I}_8 \rightarrow ^5\text{F}_3$

Table 4.5: Excitation peaks of Ho^{3+} - Gd^{3+} doped Y_2O_3 samples and their respective transitions while monitoring 548 nm λ_{Em} .

The excitation wavelengths at 309 and 313 nm (enlarged in Figure 4.6 a.) only generates peaks in the samples with Gd^{3+} ions. These peaks can therefore be assigned to the $^6\text{P}_{5/2}$ and $^6\text{P}_{7/2}$ states of Gd^{3+} . They are most probably the result of ET towards the states of Ho^{3+} , and then vibrationally relax towards the intermediate where radiative emission occurs towards the ground state. This is supported by the fact that Ho^{3+} does not have energy states in those wavelengths according to the Dieke Diagram (Figure 2.2). The intensity of these peaks decreases as the Gd^{3+} concentration increases which can be explained by concentration quenching of Gd^{3+} ions. Furthermore, the excitation peak at 448 nm (which is the $^5\text{G}_6$ state) was found to be an excellent match of the ~450 nm excitation wavelength for the blue-to-UVB UC application.

Using the excitation wavelength of 448 nm determined in Figure 4.6 a. The emission spectra in Figure 4.6 b. was acquired. It shows one sharp and intense peak at 548 nm. This peak belongs to the emission from closely spaced $^5\text{F}_4$ and $^5\text{S}_2$ states towards the $^5\text{I}_8$ ground state of Ho^{3+} . Its intensity is strongly dominating over the other emission peaks of Ho^{3+} ($^5\text{F}_3, ^5\text{F}_5 \rightarrow ^5\text{I}_8$ and $^5\text{S}_2 \rightarrow ^5\text{I}_7$). The Ho^{3+} emission from the intermediate ($^5\text{F}_4$ and $^5\text{S}_2$) has the reoccurring trend as in the excitation spectrum that is in the decreasing order of 0, 10, 25, 99.5% Gd^{3+} . The strong emission of the $^5\text{F}_4$ and $^5\text{S}_2$ intermediate states is promising as it will result in a more efficient ETU towards other Ho^{3+} ions.

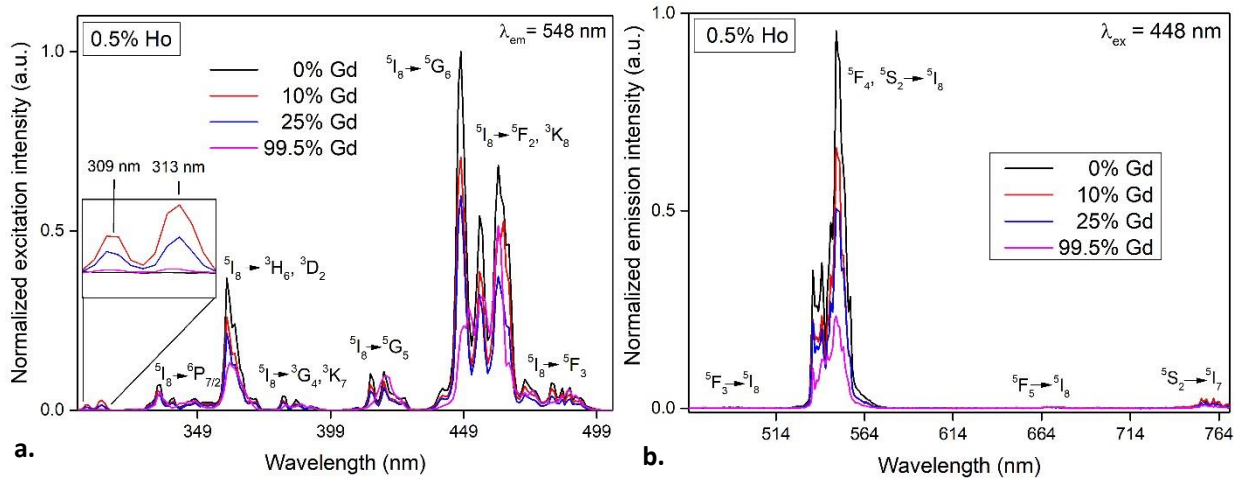


Figure 4.6: Photoluminescence spectra of Y_2O_3 : 0.5% Ho, $y\%$ Gd (with $y = 0, 10, 25$ and 99.5% Gd.) **a.** Excitation scanned from 305–505 nm and **b.** Emission spectra scanned from 465–770 nm.

To investigate the optimal concentration for population of the Blue-to-UVB UC intermediate state of Ho^{3+} , excitation and emission of other dopant concentrations were investigated. The emission graphs (Figure 4.7 **a.**) from left to right are the 0.5, 1 and 3% Ho^{3+} doped samples and in each Ho^{3+} concentration, the Gd^{3+} concentration was varied. These emission graphs are focused on the ~ 548 nm ($^5\text{F}_4$ and $^5\text{S}_2$) emission peak. This peak generally shrinks with the increase of Ho^{3+} concentration and increase of the Gd^{3+} concentration.

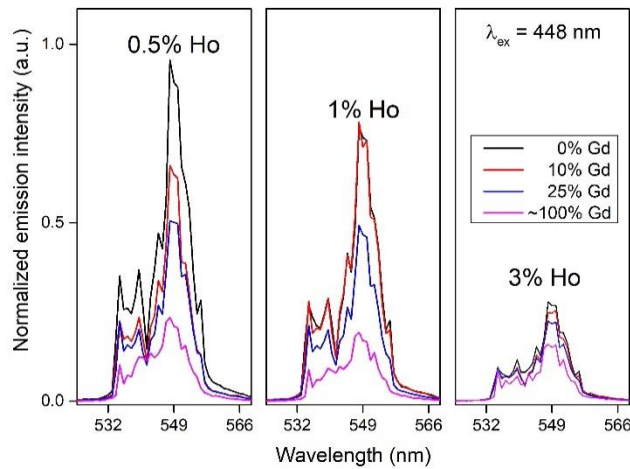


Figure 4.7: Emission spectra of the $^5\text{F}_4$ and $^5\text{S}_2$ states towards the $^5\text{I}_8$ ground state of various concentrations of Y_2O_3 : 0.5% Ho, $y\%$ Gd (with $y = 0, 10, 25$ and $\sim 100\%$ Gd).

The trend of the decrease in the emission intensity due to increase of dopant concentrations is the same for every concentration which indicates strong concentration quenching above the 0.5% Ho^{3+} and 10% Gd^{3+} dopant concentration. In the Ho^{3+} - Gd^{3+} system, there is the possibility of cross-relaxation between the Ho^{3+} ions such as depicted in Figure 2.7 **c.**⁴² The excitation spectra for the 1% and 3% Ho concentration exhibit the same trend which were expected. These can be found in Appendix B.

Blue-to-UVB UC has been measured in the $\text{Ho}^{3+}\text{-Gd}^{3+}$ samples excited by the 448 nm wavelength which can be seen in Figure 4.8. The graphs are focused on the 313 nm blue-to-UVB UC peak scanned from 260 to 330 nm. In Figure 4.8 **a.**, the comparison of this peak between the concentrations of the first exploration are put next to each other. There is a small peak at the lower wavelength 308 nm, followed by the much more intense 313.5 nm peak. Only the samples containing 10 and 25% Gd^{3+} generates a strong peak and the $\sim 100\%$ Gd^{3+} generates a small negligible peak, only visible when zoomed in. The 0% Gd^{3+} concentration sample does not show anything. The reoccurring trend of the decrease of this peak with increasing Ho^{3+} concentration is observed.

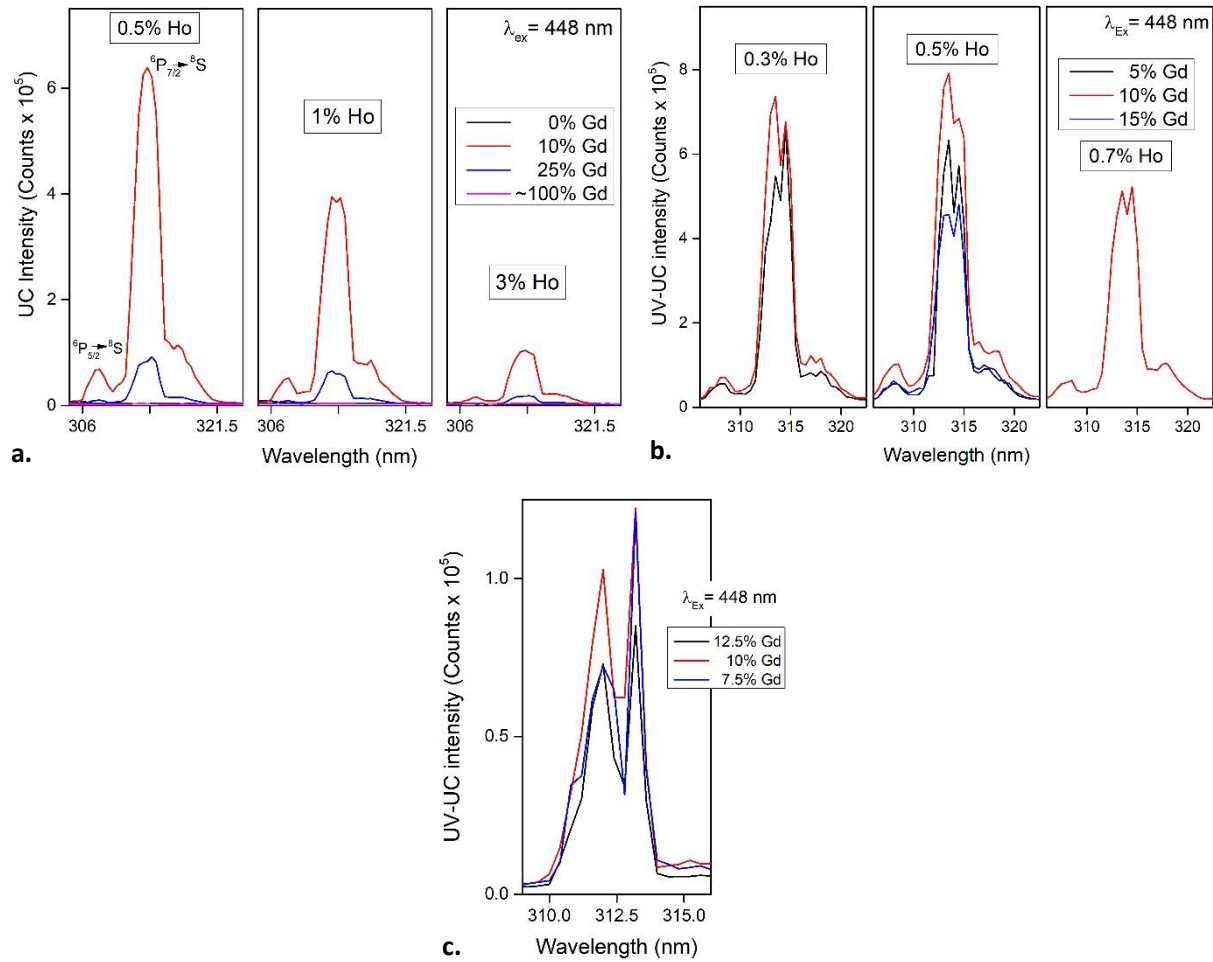


Figure 4.8: Blue-to-UVB UC graphs of the prepared Y_2O_3 : $x\%$ Er^{3+} , $y\%$ Gd^{3+} samples with ($\lambda_{\text{ex}} = 448$ nm) focused on the 313 nm emission peak of Gd^{3+} in **a.** $x=0.5, 1$ and 3% , $y=0, 10, 25$ and $\sim 100\%$ in **b.** $x=0.3, 0.5$ and 0.7% , $y=5, 10$ and 15% in **c.** $x=0.5\%$, $y=7.5, 10, 12.5\%$

The peaks at 308 and 313.5 nm are attributed to the $^6\text{P}_{5/2}$ and the $^6\text{P}_{7/2}$ emission states of Gd^{3+} respectively. The fact that only the samples containing Gd^{3+} show this peak indicate that Ho^{3+} does not have emission states in this wavelength which is confirmed by the Dieke diagram. The decrease of the 313.5 nm peak is mainly due to concentration quenching of the Ho^{3+} ion towards a defect. Moreover, the energy back transfer which was observed in the excitation measurements (Figure 4.6) due to increase of Gd^{3+} concentration contributes slightly. This energy back transfer should be small considering the low intensity of the 309 and 313 nm excitation peak. The 0.5% Ho^{3+} and 10% Gd^{3+} concentration has the highest peak and is therefore the most efficient in blue-to-UVB UC.

Similar to the Er^{3+} samples, the dopant concentrations have been optimized for $\text{Ho}^{3+}\text{-Gd}^{3+}$. In the first exploration in Figure 4.8 **a**. 0.5% Ho in combination with 10% Gd was found to have the most efficient blue-to-UVB UC. This concentration was further narrowed down in Figure 4.8 **b**. and **c**. In **b**. the concentrations of 0.3, 0.5 and 0.7% Ho^{3+} are plotted next to each other. The 308 and 313.5 nm peaks of the resp. ${}^6\text{P}_{5/2}$ and ${}^6\text{P}_{7/2}$ states were observed in every sample in the same manner as in Figure 4.8 **a**. A decrease or increase of the Gd^{3+} concentration from 10 to 5 or 15% decreases the blue-to-UVB UC intensity. When the 0.5% Ho decreases to 0.3% or increases to 0.7% the efficiency decreases. In Figure 4.8 **c**. the concentration is explored by narrowing down even more, resulting in 0.5% Ho^{3+} with 7.5, 10 and 12.5 % Gd^{3+} samples. Finally, in some of the 313 nm UC peaks, a double peak instead of only one is observed, this is expected as there is crystal field splitting of the ${}^6\text{P}$ state, resulting in multiple degeneracies. The fact that the double peaks is not observed in every 313 nm UC peak could be due to inconsistencies of the Oportek HE 355II laser because the laser is not always stable. After optimizing the concentration for blue-to-UVB UC efficiency, it could be concluded that the 0.5% Ho^{3+} and 10% Gd^{3+} is the most efficient concentration for blue-to-UVB UC in Y_2O_3 .

In addition to the $\text{Er}^{3+}\text{-Gd}^{3+}$ microcrystalline results, Y_2O_3 samples doped with the $\text{Ho}^{3+}\text{-Gd}^{3+}$ couple were successfully synthesized with various dopant concentrations. This was proven by the assessment of the morphology (XRD) and photoluminescence (excitation and emission) in Figure 4.1 and Figure 4.6 respectively. Blue-to-UVB UC was successfully observed and optimized in which the highest blue-to-UVB UC intensity was found to be 0.5% Ho^{3+} with 10% Gd^{3+} . Concentration quenching was found to be strong quenching mechanisms of the 313 nm UC emission intensity in $\text{Ho}^{3+}\text{-Gd}^{3+}$ doped Y_2O_3 . A summary of the results can be found in Table 4.6.

Dopants in Y_2O_3	Ho^{3+} & Gd^{3+}
Intermediate state level	${}^5\text{F}_4/{}^4\text{S}_2$ (548 nm)
Most efficient λ_{Ex}	448 nm
Most efficient UC Concentration	Y_2O_3 : 0.5% Ho^{3+} , 10% Gd^{3+}

Table 4.6: Summarized results of the explored microcrystalline $\text{Ho}^{3+}\text{-Gd}^{3+}$ doped Y_2O_3 .

4.1.3 Time resolved measurements

To assess the quenching of the blue-to-UVB UC in the $\text{Er}^{3+}\text{-Gd}^{3+}$ and $\text{Ho}^{3+}\text{-Gd}^{3+}$ doped microcrystalline Y_2O_3 particles, decay measurements were performed by measuring the lifetime of the upconversion emission (313 nm) of Gd^{3+} ($^6\text{P}_{7/2} \rightarrow ^8\text{S}$). The results are depicted in Figure 4.9 which includes the multi-exponential decay fits. The average lifetimes were calculated by using the parameters a_i and τ_i generated by the multi-exponential fit.

As expected, the emission of lanthanide-doped upconversion particles have long lifetimes in the range of milliseconds.⁴³ In the $\text{Er}^{3+}\text{-Gd}^{3+}$ samples (Figure 4.9 a.), the lifetime of the 313 nm peak is the longest in the lowest Gd^{3+} concentration (2.5%). This lifetime decreases upon increasing the Gd^{3+} concentration as can be seen in the red (5% Gd^{3+}) and blue (10% Gd^{3+}) decay-curves. It is interesting that the lifetime halves when the concentration of Gd^{3+} doubles ($0.40 \rightarrow 0.22 \rightarrow 0.11$ ms). When observing the decay curves in the initial decay, the order is reversed from fastest to slowest decaying $2.5 > 5 > 10\%$ Gd^{3+} . Overall, the graphs look multi-exponential which means that multiple components contribute to the lifetime of the 313 nm peak.

The decrease of the lifetime by addition of Gd^{3+} is the result of concentration quenching by addition of the Gd^{3+} ions. The reversed order of decay time in the initial part was not expected. A hypothesis is that due to less Gd^{3+} ions, there are less Gd^{3+} ions in its immediate vicinity for energy migration to occur (most probably resonant radiative energy transfer because this takes more time) which makes the emission more rapid, this theory is only applicable for the first part of the decay curves. BET, cross relaxation and concentration quenching are the main contributing components of the quenching of the 313 nm emission lifetime. This causes the multi-exponential behaviour as there are multiple nonradiative decay processes involved.

The lifetime of the 312 nm emission of the 1% $\text{Ho}^{3+}\text{-Gd}^{3+}$ couple in Figure 4.9 b is at least twice as long compared to the 313 nm emission of $\text{Er}^{3+}\text{-Gd}^{3+}$. A decrease of the lifetime is observed as the Gd^{3+} dopant increases in the order of $7.5 > 10 > 12.5\%$ Gd. The decay curves exhibit a more mono-exponential behaviour since they have a straighter line than the ones of $\text{Er}^{3+}\text{-Gd}^{3+}$.

Due to increasing Gd^{3+} , energy migration towards other Gd^{3+} ions and BET could become more probable. A reason for significant worse efficiency of the $\text{Er}^{3+}\text{-Ho}^{3+}$ system is that there is a higher probability of BET from the emitting $^6\text{P}_{7/2}$ state of Gd^{3+} to the $^2\text{P}_{3/2}$ state of Er^{3+} meaning that the $\text{Ho}^{3+}\text{-Gd}^{3+}$ couple experiences less quenching. An additional reason for the multi-exponential behaviour for both systems is that the dopants are randomly distributed in the crystal lattice.³⁰ Conclusively, the $\text{Ho}^{3+}\text{-Gd}^{3+}$ is more efficient for blue-to-UV UC than the $\text{Er}^{3+}\text{-Gd}^{3+}$ couple due to less quenching.

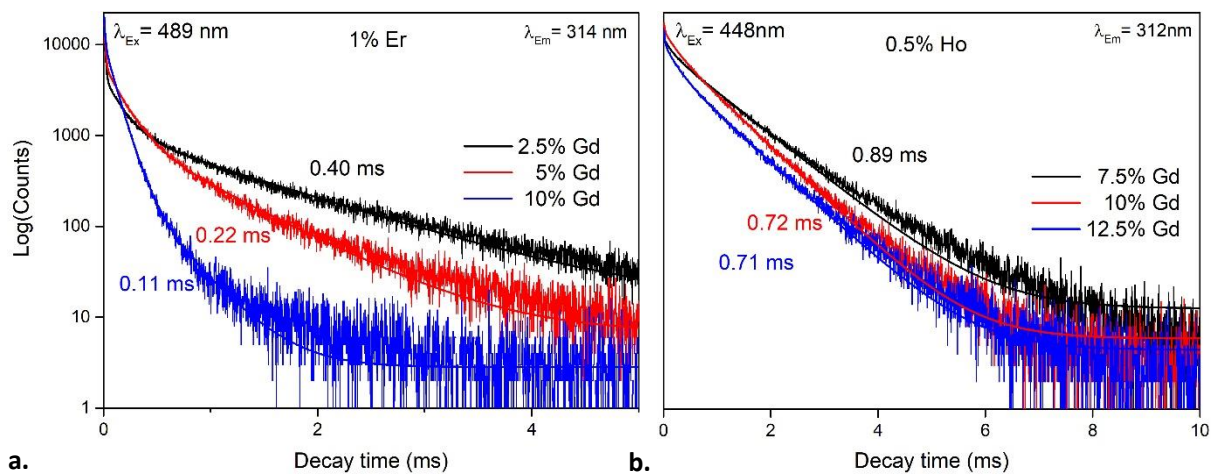


Figure 4.9: Decay time graphs of: **a.** 1% Er, $y\%$ Gd with $y = 2.5$ (black), 5 (red), and 10% (blue), **b.** 0.5% Ho, $y\%$ Gd with $y = 7.5$ (black), 10 (red) and 12.5% (blue).

4.1.4 Influence of calcination temperature

During the morphology study of the microcrystalline particles using XRD, recalcining at higher temperature was performed to find out if the temperature of 1200°C and duration of 3 h was enough to form the phase pure Y_2O_3 lattice. No significant changes in the crystal structure were observed when comparing the XRD of calcination at 1200°C for 3 h and recalcining at 1500°C for 3 h in Figure 4.2.

To assess if the optical properties were influenced by the recalcination, blue-to-UVB UC of the samples were measured before and after the second treatment which are plotted in Figure 4.10. In these graphs we can see the upconversion emission peak at 313 nm for both 1, 3 and 7% Er^{3+} and for 0.5, 1 and 3% Ho^{3+} . For both dopant couples, there is no significant change in the upconversion intensity after a 1500°C recalcining step.

As there is no notable difference in the blue-to-UVB UC intensity, it can be concluded that the initial calcination treatment of 1200°C for 3 h is enough. There is no improvement in the upconversion efficiency or additional influences in the microcrystalline samples.

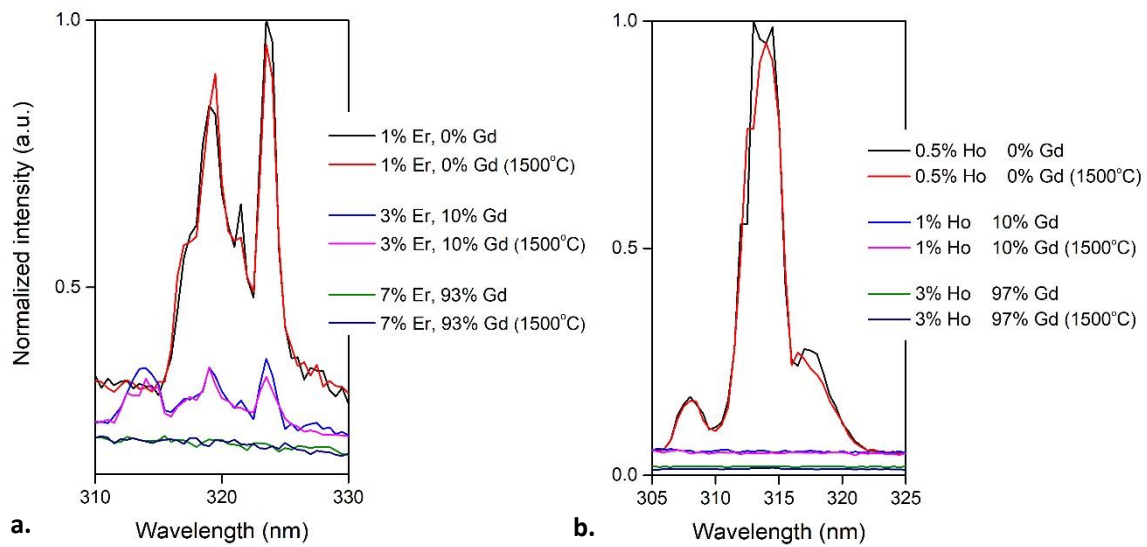


Figure 4.10: Blue-to-UVB UC measurements of **a.** $\text{Y}_2\text{O}_3: x\% \text{Er}, y\% \text{Gd}^{3+}$ and **b.** $\text{Y}_2\text{O}_3: x\% \text{Ho}, y\% \text{Gd}^{3+}$ samples after the first calcination treatment at 1200°C and after recalcining at 1500°C.

4.1.5 Summary & comparison

Blue-to-UVB UC was successfully obtained in the $\text{Er}^{3+}\text{-Gd}^{3+}$ and $\text{Ho}^{3+}\text{-Gd}^{3+}$ doped microcrystalline Y_2O_3 samples in which the concentrations were optimized for the blue-to-UVB UC efficiency. In Table 4.7 the results and findings of the microcrystalline Ln^{3+} -doped Y_2O_3 exploration is summarized.

Dopants in Y_2O_3	Er^{3+} & Gd^{3+}	Ho^{3+} & Gd^{3+}
Intermediate state level	$^4\text{S}_{3/2}$ (563 nm)	$^5\text{F}_4/^4\text{S}_2$ (548 nm)
Most efficient λ_{Ex}	489 nm	448 nm
Most efficient UC Concentration	Y_2O_3 : 1% Er^{3+} , 2.5~5% Gd^{3+}	Y_2O_3 : 0.5% Ho^{3+} , 10% Gd^{3+}
Maximum Lifetime of 313 nm emission	0.4 ms	0.89 ms

Table 4.7: Summary of the exploration on the $\text{Er}^{3+}\text{-Gd}^{3+}$ and $\text{Ho}^{3+}\text{-Gd}^{3+}$ doped microcrystalline Y_2O_3 samples.

For comparison of the blue-to-UVB UC efficiency of both the dopant couples, the blue-to-UVB UC was measured under the same conditions in Figure 4.11. In this graph, the 314 nm peak of the $\text{Ho}^{3+}\text{-Gd}^{3+}$ couple has a much stronger intensity than the 314 nm peak from $\text{Er}^{3+}\text{-Gd}^{3+}$. The blue-to-UVB UC of the $\text{Er}^{3+}\text{-Gd}^{3+}$ doped Y_2O_3 is approximately 30 times smaller.

The excitation wavelength 448 nm of the $\text{Ho}^{3+}\text{-Gd}^{3+}$ dopant couple matches really well with the desired blue excitation wavelength (450 nm) of blue-to-UVB UC application. In the lifetime measurements, this couple seems to be less influenced by quenching mechanisms as the lifetime of the 313 nm emission is about 2 times longer. Resulting from the fact that the $\text{Ho}^{3+}\text{-Gd}^{3+}$ couple had a much better blue-to-UVB UC efficiency, the focus was placed on the $\text{Ho}^{3+}\text{-Gd}^{3+}$ couple in the nanocrystalline Y_2O_3 exploration.

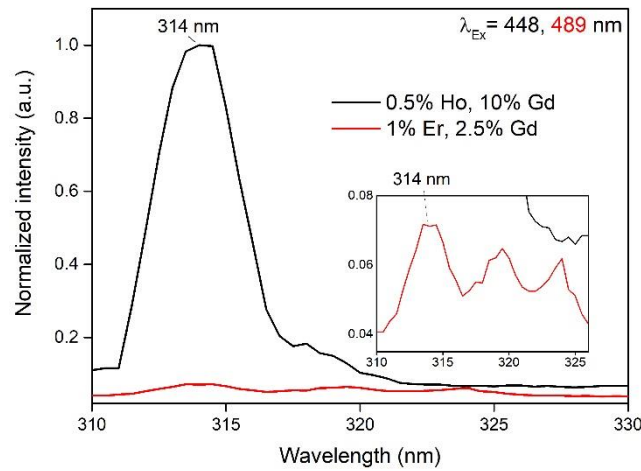


Figure 4.11: Comparison of the blue-to-UVB UC intensity of microcrystalline Y_2O_3 doped with the $\text{Ho}^{3+}\text{-Gd}^{3+}$ (black) and $\text{Er}^{3+}\text{-Gd}^{3+}$ (red) couple, recorded under identical conditions.

4.2 Nanocrystalline Y_2O_3 : 0.5% Ho, 10% Gd

After determining the most efficient Blue-to-UVB UC dopant couple and optimal concentration (0.5% Ho^{3+} -10% Gd^{3+}), nanocrystalline Y_2O_3 : 0.5% Ho^{3+} , 10% Gd^{3+} were synthesized to investigate the blue-to-UVB UC efficiency in the nanoscale regime. To achieve this goal, a few synthesis methods were tested to synthesize the nanocrystalline Y_2O_3 doped with 0.5% Ho^{3+} and 10% Gd^{3+} . Many attempts have been made to synthesize the crystal structure without using the time-consuming calcination treatment.

4.2.1 Results of Method A (RE-Carbonates)

NPs were synthesized using method A (Ligands: oleic acid and oleylamine, heating at 280°C for 30 min). To assess the influence of the calcination treatment on the crystal structure, XRD diffractograms were taken of before and after the treatment. These are plotted in Figure 4.12 in which red is the phase pure Y_2O_3 reference and the dark grey is the bare aluminium sample holder. The diffractogram of the NPs before the calcination does not correspond to a pure crystalline structure. After the calcination treatment at 800°C for 3 h, the diffractogram shows characteristic peaks for the phase pure cubic Y_2O_3 . These peaks are broader when compared with the diffractograms of the microcrystalline Y_2O_3 in Figure 4.1 and the aluminium sample holder peaks are in this case noticeable.

The calcination treatment of the samples after synthesis resulted in the phase pure cubic Y_2O_3 lattice. The broad peaks are a result of lattice strain and small sizes of the nanoparticles. The noise in the diffractograms and appearance of the aluminium sample holder peaks is due to the small amount of powder used for the measurement in contrast to the microcrystalline XRD results. Unfortunately, synthesizing the NPs without a calcination treatment was not successful. Nevertheless, crystalline phase pure Y_2O_3 doped with 0.5% Ho-10% Gd NPs were successfully obtained by calcination.

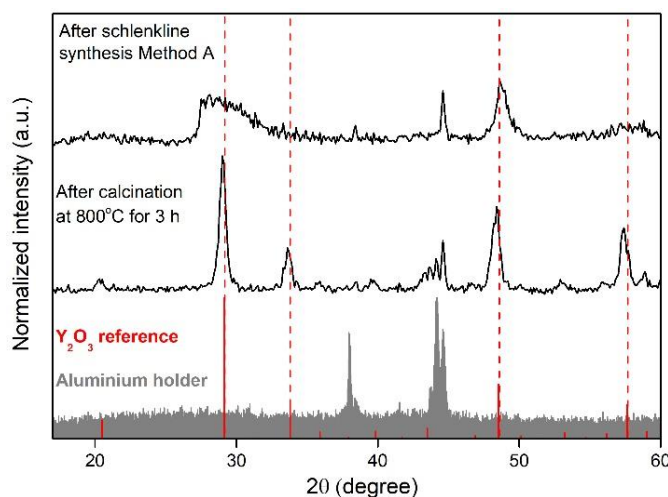


Figure 4.12: XRD spectra of Y_2O_3 :0.5% Ho, 10% Gd NPs synthesized by Method A, the crystalline Y_2O_3 phase is only formed after the calcination step. The Y_2O_3 reference peaks are plotted in (red) and the aluminium holder diffractogram in (grey).

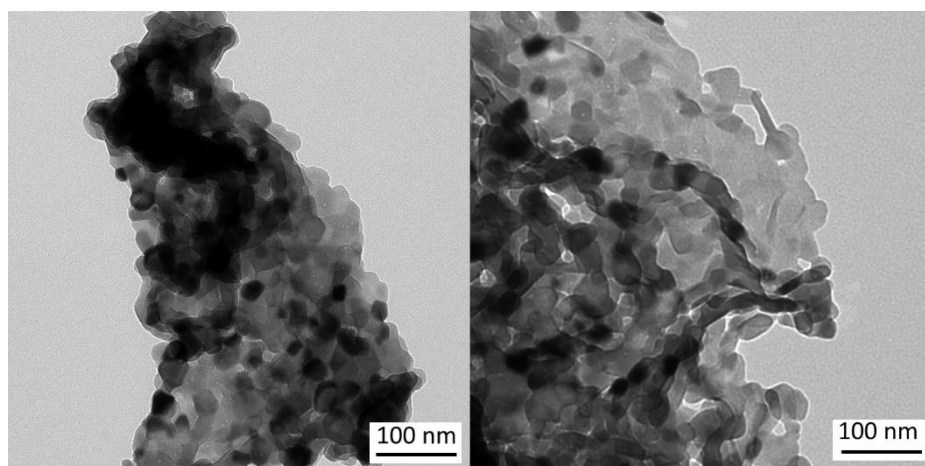


Figure 4.14: TEM images of the $\text{Y}_2\text{O}_3:0.5\% \text{ Ho}$, 10% Gd NPs synthesized using Method A.

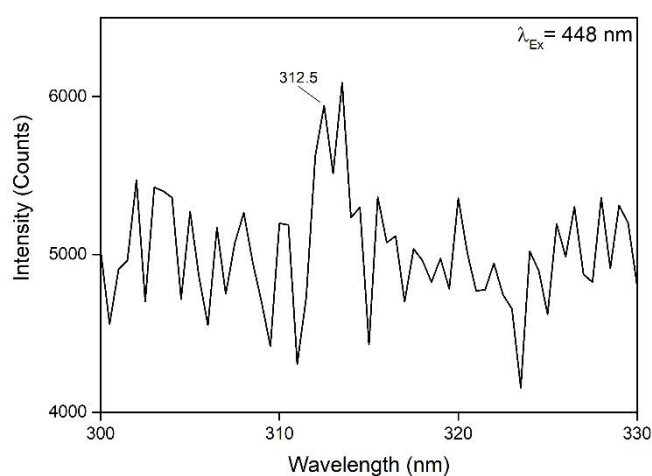


Figure 4.13: Blue-to-UVB UC of the $\text{Y}_2\text{O}_3:0.5\% \text{ Ho}$, 10% Gd NPs synthesised by Method A.

To investigate and assess the morphology of the Y_2O_3 NPs, TEM images were recorded in Figure 4.14. The particles are large (in the micrometre range) and look like clumps of many aggregated smaller particles. We can conclude that monodisperse particles are not successfully made using method A.

Although the morphology did not turn out to be desired, the optical properties were still tested. In Figure 4.13 blue-to-UVB UC was obtained from these particles using the pulsed Opotek. In this graph the 312.5 nm emission peak is hardly distinguishable from the noise which means that the size and morphology of $\text{Y}_2\text{O}_3: 0.5\% \text{ Ho}^{3+}$, 10% Gd^{3+} does play a big role on the blue-to-UVB UC efficiency. An increase in surface will give rise to many surface defects and quenching of the blue-to-UVB UC.

4.2.2 Results of Method B (RE-Chlorides)

As method A did not seem to result in monodisperse NPs, method B (Ligand: oleylamine, heating at 310°C for 1 hr) was tested, and the focus was placed on improving the morphology. After colloidal synthesis, the particles were ultrafine, meaning that we were able to see the particles jump around just by touching the glass vile that contains the particles. This which was a good indication of successful NPs synthesis. Afterwards, the NPs were calcined in various conditions (by changing the temperature and duration) for finding the parameters of controlled morphology and homogeneous sizes of the calcined NPs. The calcination temperatures ranged from 700, 800, 900 to 1000 °C and the duration ranged from 0.5 till 4 h in steps of 30 min.

The calcined samples resulted in similar and phase pure cubic Y_2O_3 crystallinity which was verified from the XRD diffractogram of selected samples in Figure 4.15. The diffractograms of the NPs show single phase cubic Y_2O_3 lattice. The aluminium sample holder peaks were also observed.

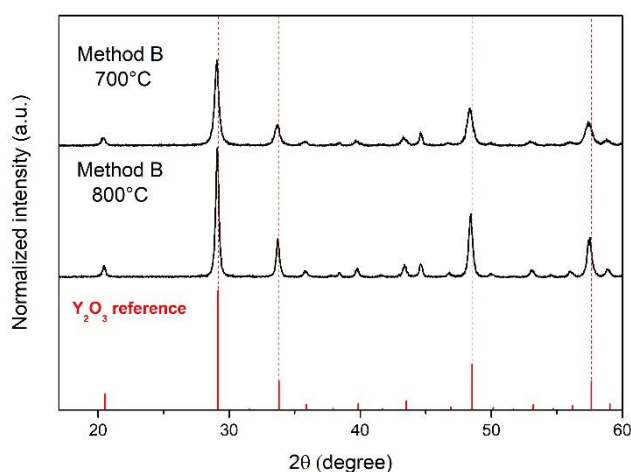


Figure 4.15: Diffractogram of selected $\text{Y}_2\text{O}_3:0.5\% \text{Ho}^{3+}, 10\% \text{Gd}^{3+}$ samples of Method B calcined at 700 and 800°C for 3 h including a Y_2O_3 reference spectrum in red.

TEM images were taken for the synthesized samples at different calcination temperatures and different durations. However, in a few samples did we see the particles on the TEM grids while taking the TEM images. This was not understood, and multiple dispersing solvents and sonication steps were tested without improvements. TEM images of the NPs of before the calcination treatment are depicted in Figure 4.17. These NPs are spherical and well-monodisperse with an average diameter of ~8 nm. which is a good result for further exploration. Other TEM images with visible particles can be found in Appendix C.

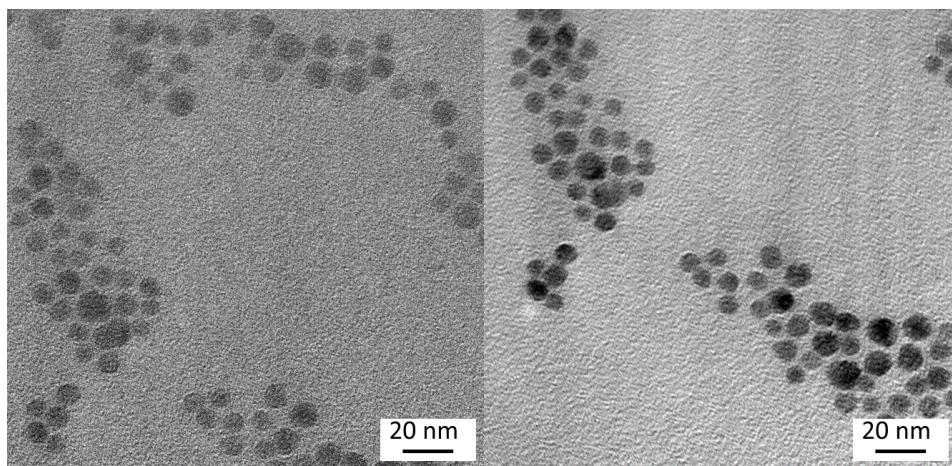


Figure 4.17 TEM images of $\text{Y}_2\text{O}_3:0.5\% \text{Ho}^{3+}$, $10\% \text{Gd}^{3+}$ NPs synthesized by Method B before calcination.

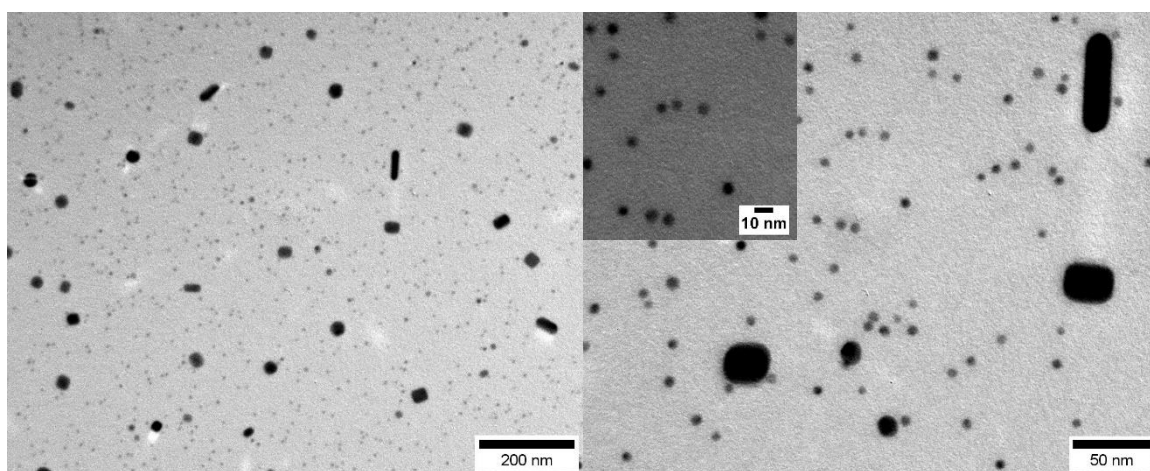


Figure 4.16: TEM images of $\text{Y}_2\text{O}_3:0.5\% \text{Ho}^{3+}$, $10\% \text{Gd}^{3+}$ NPs synthesized by Method B calcined at 800°C for 3 h.

A mixture of monodisperse individual crystalline particles were only obtained by calcining the NPs at 800°C for 3 h. This resulted in a mixture of particles with different of shapes and sizes as can be observed in the TEM images in Figure 4.16. The NPs are a dispersion of rod-like, cubic and spherical NPs. The smallest NPs have a diameter of ~ 6 nm, the cubes are ca. 30×30 nm, the rods are ca. 70×18 nm and the big spheres ca. 29 nm. In the NPs that were calcined at higher temperatures, the particles aggregated and resulted in a similar structure like in Figure 4.14 (see Appendix C).

The dispersion of the different structures is surprising, and it is not clear to how these are formed. The smallest particles are presumably the same ones as the NPs before calcination in Figure 4.17 which seem have shrunk from 8 to 6 nm. This could happen due to crystal lattice formation and therefore compressing and shrinking the particle. This indicates that calcining the NPs at this temperature can form crystalline monodisperse particles.

4.2.3 Results of Method C (RE-Nitrates)

To assess the size dependency of the blue-to-UVB UC efficiency, method C (homogeneous precipitation, heating till 85°C for 2 h) was used to synthesize large monodisperse spherical $\text{Y}_2\text{O}_3:0.5\% \text{Ho}$, 10% Gd NPs. In the TEM images of these NPs in Figure 4.18, good monodisperse spherical particles are observed. The average diameter of the NPs is ca. 250 nm which is much bigger than the ones synthesized in Method B (Figure 4.16). The XRD diffractogram in Figure 4.19 indicates a phase pure cubic Y_2O_3 lattice. Thus, large spherical and monodisperse $\text{Y}_2\text{O}_3:0.5\% \text{Ho}$, 10% Gd NPs were successfully synthesized using this method.

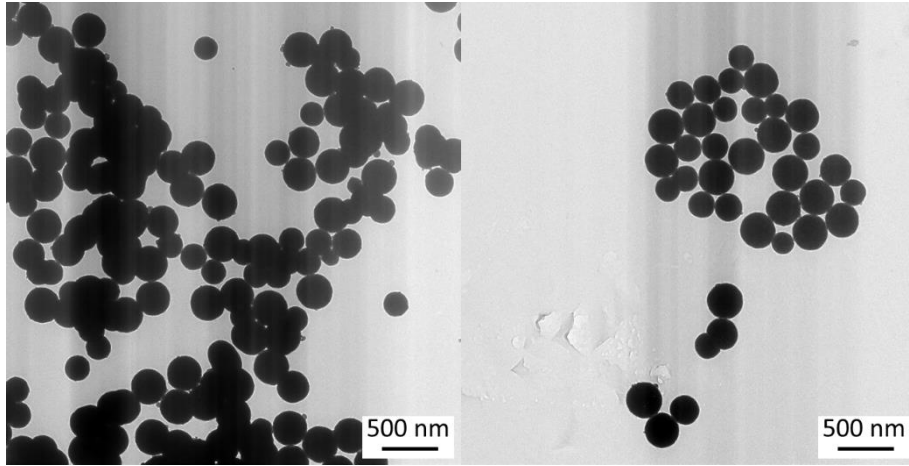


Figure 4.18: TEM images of the $\text{Y}_2\text{O}_3:0.5\% \text{Ho}^{3+}$, 10% Gd^{3+} NPs synthesized by Method C calcinated at 800°C for 3 h.

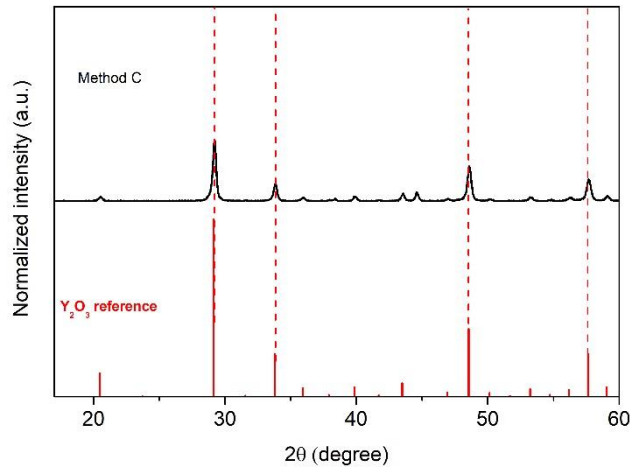


Figure 4.19: XRD diffractogram of the $\text{Y}_2\text{O}_3:0.5\% \text{Ho}^{3+}$, 10% Gd^{3+} NPs synthesized by Method C including a Y_2O_3 reference spectrum in red.

4.2.4 Optical results, summary & comparison

$\text{Y}_2\text{O}_3:0.5\% \text{ Ho}$, 10% Gd NPs were synthesized to assess the blue-to-UVB UC efficiency at the nanoscale. Three different methods were explored to synthesize monodisperse $\text{Y}_2\text{O}_3:0.5\% \text{ Ho}$, 10% Gd NPs. Each method resulted in NPs with different morphology as summarized in Table 4.8. Method A (Ligands: oleic acid and oleylamine, heating at 280°C for 30 min) resulted in an aggregation of particles without a defined morphology and therefore this sample is not used for comparison. To investigate and compare the optical properties of method B (Ligand: oleylamine, heating at 310°C for 1 hr) and C (homogeneous precipitation, heating till 85°C for 2 h) and the microcrystalline doped Y_2O_3 , blue-to-UVB UC measurements and lifetime measurements were performed for these samples under identical conditions. The blue-to-UVB UC measurements of the microcrystalline and nanocrystalline Y_2O_3 samples of methods B and C are plotted in Figure 4.20 **a**. The 314 nm peak has the most intensity in the microcrystalline Y_2O_3 and it decreases strongly when the size is decreased until the NPs size in Method B (~ 250 nm). This decrease is further observed by the NPs from Method C (small spheres: ~ 6 nm, cubes: $\sim 30 \times 30$ nm, rods: $\sim 70 \times 18$ nm, big spheres: ~ 29 nm).

The quenching of the blue-to-UVB UC with decrease in size is a result of the increase of surface to volume ratio in the Y_2O_3 particles. This will lead to more surface states and therefore surface defects which quenches the Gd^{3+} emission. The chance of energy migration towards higher energy vibrations (ligands) on the surface or environment will therefore be increased which quenches the intermediate states of Ho^{3+} .³¹

Quenching is further assessed using lifetime measurements in Figure 4.20 **b**. The lifetime of the 313 nm blue-to-UVB UC emission peak decreases upon a decrease of the particle size. The microcrystalline sample has the longest decay time of ca. 0.82 ms whereas the NPs have a decay time of ca. 0.30 ms.

The decrease of the decay time is due to the previously mentioned surface quenching. More quenching components seem to contribute to the decay curves of the NPs (the shape of the curve is more bend) and consequently decreases the efficiency of the blue-to-UVB UC significantly. Nevertheless, blue-to-UVB UC was obtained in $\text{Y}_2\text{O}_3:0.5\% \text{ Ho}$, 10% Gd NPs.

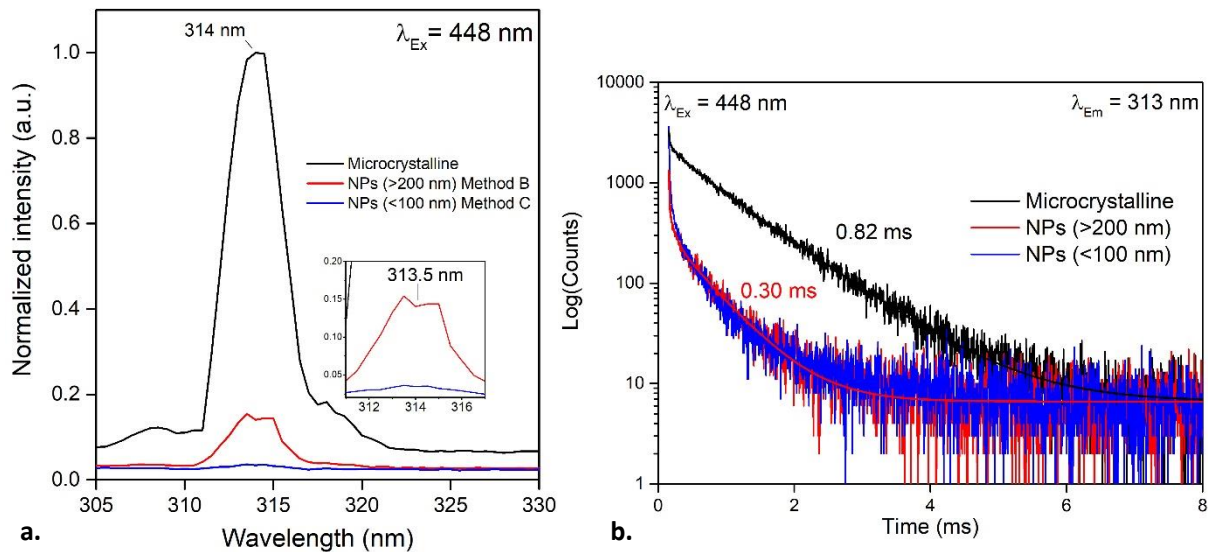


Figure 4.20: Optical properties of $\text{Y}_2\text{O}_3:0.5\% \text{ Ho}^{3+}$, 10% Gd^{3+} Microcrystalline (black) and NPs (Method C in red and Method B in blue) **a**. Blue-to-UVB UC measurements **b**. Lifetime measurements.

Samples	Microcrystalline	Method B	Method C
Y₂O₃:0.5%Ho,10% Gd			
Morphology	Bulk material	NPs (~6 nm)	NPs (~250 nm)
Dispersity		Polydisperse	Monodisperse
Blue-to-UVB UC normalized intensity	1	0.15	0.036
Decay time	~0.8 ms	~0.30 ms	~0.30 ms

Table 4.8: Summary of the exploration of Y₂O₃:0.5% Ho³⁺, 10% Gd³⁺ micro- and nanoparticles results.

5. Conclusions & Outlook

In this work, a new host material (Y_2O_3) for Blue-to-UVB UC was investigated using the lanthanide couples: Er^{3+} - Gd^{3+} and Ho^{3+} - Gd^{3+} . These were successfully synthesized in both microcrystalline and nanocrystalline confirmed by XRD and photoluminescence measurements. Furthermore, successful (~ 450 nm) blue-to-UVB (~ 313 nm) UC was realised for both lanthanide dopant couples in microcrystalline and for the Ho^{3+} - Gd^{3+} couple also in nanocrystalline.

Microcrystalline lanthanide-doped Y_2O_3 samples were synthesized by the “wet chemistry” precipitation technique using oxalic acid. The optimal concentration for blue-to-UVB UC efficiency were first assessed in these microcrystalline particles. During the research, it was found that the Ho^{3+} - Gd^{3+} lanthanide couple resulted in much higher blue-to-UVB UC efficiency than the Er^{3+} - Gd^{3+} couple. The Er^{3+} - Gd^{3+} couple had more quenching due to the presumably higher BET and cross-relaxation probabilities. In addition, the highest blue-to-UVB UC efficiency were found to be generated by the Y_2O_3 : 1% Er^{3+} , 2.5/5% Gd^{3+} and the Y_2O_3 : 0.5% Ho^{3+} , 10% Gd^{3+} sample for the Er^{3+} - Gd^{3+} and Ho^{3+} - Gd^{3+} couples respectively.

Y_2O_3 NPs doped with 0.5% Ho^{3+} -10% Gd^{3+} were synthesized using 3 colloidal methods (A, B and C) using different dopant precursors and conditions. Blue-to-UVB Upconverting NPs were obtained in each method. Method A (RE-Carbonates) resulted in completely aggregated particles. The methods B (RE-Chlorides) and C (RE-Nitrates) resulted in individual particles. The NPs of method B had an interesting distribution of diverse shapes that were rod-like (70 x 18 nm), cubical (30 x 30 nm), big spheres (~ 29 nm) and a large amount of small ~ 6 nm spheres. Method C resulted in monodisperse large spherical ~ 250 nm particles.

Blue-to-UVB UC efficiencies were compared of each sample. The highest blue-to-UVB UC efficiency was found in the microcrystalline particles. This was followed by the largest NPs from method C and then the smallest NPs of method B. Moreover, the decay curves revealed that the lifetime of the Gd^{3+} 313 nm emission peak strongly decreased. This is due to its increased surface-to-volume ratio which created more quenching agents.

In further work, the morphology of the NPs of method B can be improved by optimizing the various synthesis parameters. To improve the blue-to-UVB UC efficiency, core-shell structures to passivate the surface or attaching ligand dyes for enhancing the absorption are possible options. Finally, the dye-binding work could result in higher blue-to-UVB UC efficiency for the proposed phototherapy.

6. Acknowledgements

For my master thesis I had chosen the Condensed Matter and Interfaces (CMI) group, during the past year I have learned many things; mainly how to arrange and conduct my own experiments and the way to analyse and interpret experimental results. In addition, I have gained many valuable experiences, from organising and setting up an escape room together with Kelly, to presenting my own work in a poster at my first conference at CHAINS2018. These have been educational and enjoyable experiences that I will never forget.

I would like to express my deepest thanks to Andries Meijerink for giving me the opportunity to do my master thesis at CMI. You helped me *a lot*, from sharing your knowledge to helping me find my internship in South Korea. Your door was always open for me to sneak in for the many questions and problems that I had. Even though you were always very busy, you could always find the time to answer me with excellent details. To me, you are an amusing, friendly and open-minded person and I will never forget the way that you tease your student by wishing him “*Veel schrijfplezier*” with a grin while you were on your way home to enjoy the weekend.

Dechao, thank you for your supervision during my project and the life lessons that I gained from you. You were considerate and patient with me and your trust gave me freedom in doing this project. You were always on stand-by for any question or problem that I had, in person, text messaging and even when you were on holidays in China. Besides, we spend good times outside of CMI together with Georgia and Liudmyla. We went to the movies, had a pizza party, went to the Rijksmuseum and had Dim Sum in Amsterdam. I have undoubtedly enjoyed spending my time as your student.

Finally, I would like to thank Kelly, Dirk-Floris, Tomas, Nicolette, Georgia, Jurre, Jesper, Jos, Jan and Naud for the fun conversations that we had in the master room, thank you Peter Jacobse for the occasional “*wiener melange*” breaks and I really appreciated the PhD candidates, postdocs and supporting staff in CMI for creating a warm, friendly and enjoyable atmosphere.

7. References

1. Powell, F. C. & Dicken, C. H. Psoriasis and vitiligo. *Acta Derm. Venereol.* **63**, 246–249 (1983).
2. Parrish, J. A. & Jaenicke, K. F. Action spectrum for phototherapy of psoriasis. *J. Invest. Dermatol.* **76**, 359–362 (1981).
3. Berneburg, M., Röcken, M. & Benedix, F. Phototherapy with narrowband vs broadband UVB. *Acta Derm. Venereol.* **85**, 98–108 (2005).
4. Reich, A. & Medrek, K. Effects of narrow band UVB (311 nm) irradiation on epidermal cells. *Int. J. Mol. Sci.* **14**, 8456–8466 (2013).
5. W, B. T. A Practical Approach to Home UVB Phototherapy for the Treatment of Generalized Psoriasis. *Pr. Dermatol* **7**, 31–35 (2010).
6. Pfaff, S., Born, M. & Merk, F. Prospective Randomized Long-Term Study on the Efficacy and Safety of UV-Free Blue Light for Treating Mild Psoriasis Vulgaris. 24–34 (2015). doi:10.1159/000430495
7. Wilhelm, S. Perspectives for Upconverting Nanoparticles. *ACS Nano* **11**, 10644–10653 (2017).
8. Van Der Ende, B. M., Aarts, L. & Meijerink, A. Lanthanide ions as spectral converters for solar cells. *Phys. Chem. Chem. Phys.* **11**, 11081–11095 (2009).
9. Wen, S. *et al.* Advances in highly doped upconversion nanoparticles. *Nat. Commun.* **9**, (2018).
10. Geitenbeek, R. G. *et al.* NaYF₄:Er³⁺,Yb³⁺/SiO₂ Core/Shell Upconverting Nanocrystals for Luminescence Thermometry up to 900 K. *J. Phys. Chem. C* **121**, 3503–3510 (2017).
11. Giedraityte, Z., Tuomisto, M., Lastusaari, M. & Karppinen, M. Three- and Two-Photon NIR-to-Vis (Yb , Er) Upconversion from ALD / MLD-Fabricated Molecular Hybrid Thin Films. *ACS Appl. Mater. Interfaces* **10**, 8845–8852 (2018).
12. Liu, S.-J., Liu, H., Lü, Y.-H. & Sang, Y.-H. Preparation of Y₂O₃ nanoparticles and transparent ceramics by homogeneous precipitation method. *Gongneng Cailiao/Journal Funct. Mater.* **40**, 6–8 (2009).
13. Dong, H., Sun, L. D. & Yan, C. H. Energy transfer in lanthanide upconversion studies for extended optical applications. *Chem. Soc. Rev.* **44**, 1608–1634 (2015).
14. Gómez, S. Y., Da Silva, A. L., Gouvêa, D., Castro, R. H. R. & Hotza, D. Nanocrystalline yttria-doped zirconia sintered by fast firing. *Mater. Lett.* **166**, 196–200 (2016).
15. Wang, X. *et al.* Dye-sensitized lanthanide-doped upconversion nanoparticles. *Chem. Soc. Rev.* **46**, 4150–4167 (2017).
16. Materials, L., Hanninen, P., "rma, "nninen ? Harri Ha, Edition, T. & Curie, D. *Luminescent Materials - Blasse and Grabmaier - 1994.pdf. Springer Series on Fluorescence, Vol. 7* (2011). doi:10.1007/978-3-642-21023-5
17. Cotton, S. *Lanthanide and Actinide Chemistry and Spectroscopy. American Chemical Society* (2006). doi:10.1002/0470010088
18. Dieke, G. H., Crosswhite, H. M. & Dunn, B. Emission Spectra of the Doubly and Triply Ionized Rare Earths*. *J. Opt. Soc. Am.* **51**, 820 (1961).
19. Walsh, B. M. Judd-Ofelt theory: principles and practices. in *Advances in Spectroscopy for Lasers and Sensing* (2006). doi:10.1007/1-4020-4789-4_21
20. Atkins, P. W. *Shriver & Atkins' inorganic chemistry. Oxford University Press* (2010). doi:978-0-19-926463-6
21. Tanner, P. A. Some misconceptions concerning the electronic spectra of tri-positive europium and cerium. *Chem. Soc. Rev.* **42**, 5090–5101 (2013).

22. Haase, M. & Schafer, H. Upconverting nanoparticles. *Angew. Chem. Int. Ed.* **50**, 5808–5829 (2011).
23. Joubert, M. 1-s2.0-S0925346798000433-main.pdf. **11**, (1999).
24. Joubert, M. F. Photon avalanche upconversion in rare earth laser materials. *Opt. Mater. (Amst.)* **11**, 181–203 (1999).
25. Shang, Y., Hao, S., Yang, C. & Chen, G. Enhancing Solar Cell Efficiency Using Photon Upconversion Materials. *Nanomaterials* **5**, 1782–1809 (2015).
26. Dexter, D. L. A theory of sensitized luminescence in solids. *J. Chem. Phys.* **21**, 836–850 (1953).
27. Forster, T. Energiewanderung und Fluoreszenz. *Naturwissenschaften* (1946). doi:10.1007/BF00585226
28. Guo, H. *et al.* Visible upconversion in rare earth ion-doped Gd₂O₃ nanocrystals. *J. Phys. Chem. B* **108**, 19205–19209 (2004).
29. Li, X., Zhang, F. & Zhao, D. Lab on upconversion nanoparticles: Optical properties and applications engineering via designed nanostructure. *Chem. Soc. Rev.* **44**, 1346–1378 (2015).
30. Rabouw, F. T. *et al.* Quenching Pathways in NaYF₄:Er³⁺,Yb³⁺Upconversion Nanocrystals. *ACS Nano* **12**, 4812–4823 (2018).
31. Wang, Z. & Meijerink, A. Concentration Quenching in Upconversion Nanocrystals. *J. Phys. Chem. C* **122**, 26298–26306 (2018).
32. Auzel, F. Upconversion processes in coupled ion systems. *J. Lumin.* **45**, 341–345 (1990).
33. Carnall, W. T., Fields, P. R. & Rajnak, K. Electronic energy levels of the trivalent lanthanide aquo ions. IV. Eu³⁺. *J. Chem. Phys.* **49**, 4424–4442 (1968).
34. Shen, D. *et al.* Room temperature continuous-wave laser performance of LD pumped Er:Lu₂O₃ and Er:Y₂O₃ ceramic at 27 μm. *Opt. Express* **22**, 19495 (2014).
35. Lakowicz, J. R. *Principles of fluorescence spectroscopy. Principles of Fluorescence Spectroscopy* (2006). doi:10.1007/978-0-387-46312-4
36. De Mello Donegá, C. *Nanoparticles: Workhorses of nanoscience. Nanoparticles: Workhorses of Nanoscience* (2014). doi:10.1007/978-3-662-44823-6
37. Pahari, B. *et al.* Biophysical Characterization of Genistein in Its Natural Carrier Human Hemoglobin Using Spectroscopic and Computational Approaches. *Food Nutr. Sci.* **2013**, 83–92 (2013).
38. Sohn, S., Kwon, Y., Kim, Y. & Kim, D. Synthesis and characterization of near-monodisperse yttria particles by homogeneous precipitation method. *Powder Technol.* **142**, 136–153 (2004).
39. LIU, Z., LI, M., HU, Y., WANG, M. & SHI, Z. Preparation of large particle rare earth oxides by precipitation with oxalic acid. *J. Rare Earths* (2008). doi:10.1016/S1002-0721(08)60057-5
40. Wang, H., Uehara, M., Nakamura, H., Miyazaki, M. & Maeda, H. Synthesis of well-dispersed Y₂O₃:Eu nanocrystals and self-assembled nanodisks using a simple non-hydrolytic route. *Adv. Mater.* **17**, 2506–2509 (2005).
41. Pan, Y. *et al.* Inherently Eu²⁺/Eu³⁺Codoped Sc₂O₃Nanoparticles as High-Performance Nanothermometers. *Adv. Mater.* **30**, 3–8 (2018).
42. Xiantao, W. E. I., Yong, L. I., Xuerui, C., Yonghu, C. & Min, Y. I. N. Strong dependence of upconversion luminescence on doping concentration in holmium and ytterbium co-doped Y₂O₃ phosphor. *J. Rare Earths* **29**, 536–539 (2011).
43. Zhou, J., Liu, Q., Feng, W., Sun, Y. & Li, F. Upconversion luminescent materials: Advances and applications. *Chem. Rev.* **115**, 395–465 (2015).

8. Appendices

A. Results of CW-laser measurements

During this research, every blue-to-UVB UC measurement was performed by the pulsed Opolette Laser. This laser is much stronger than the intended irradiance of the blue lamp for phototherapy. For this reason, the blue-to-UVB UC was assessed using a supposedly 450 nm continuous-wave (CW) laser. However, it was found that this laser was not monochromatic 450 nm. It showed strong noise near the UVB region and additional peaks which made the measurements unsuccessful. The results are plotted in the graphs below.

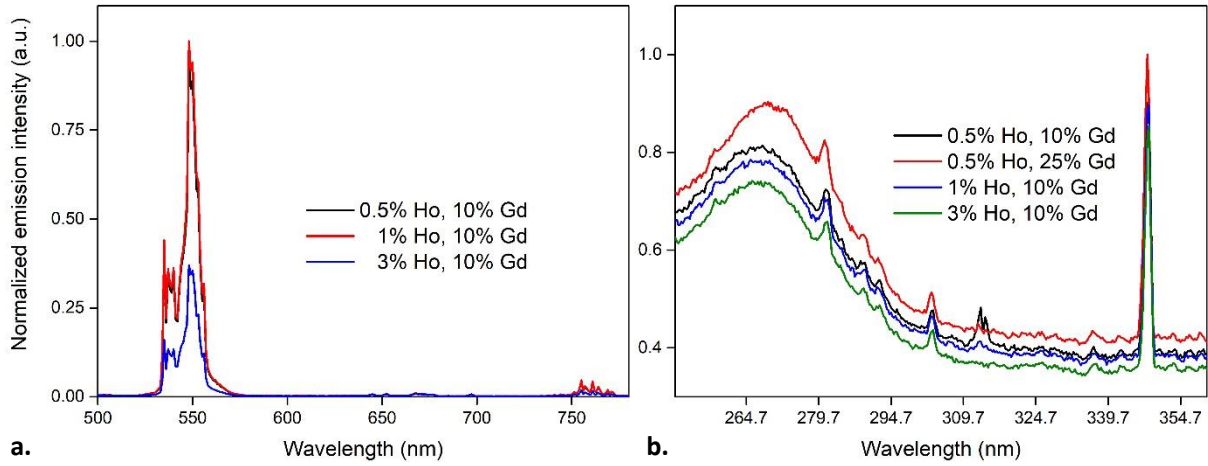


Figure 8.1: CW-laser measurements in **a.** PL emission graph of microcrystalline Y_2O_3 : x% Ho^{3+} , 10% Gd^{3+} samples. **b.** Blue-to-UVB UC graphs of microcrystalline Y_2O_3 : x% Ho^{3+} , y% Gd^{3+} samples.

The emission graph in Figure 8.1 **a.** resulted in an intense intermediate state peak of the Ho^{3+} emission. However, around the 650-700 nm a few peaks were observed which were not assignable to the emission states of Ho^{3+} . This was strange but we proceeded in doing blue-to-UVB UC measurements depicted in Figure 8.1 **b.** In this graph, strong background noise was observed in the around the 264 nm. The intense sharp peak at 347 nm could be assigned to the $^5\text{G}_3$ state of Ho^{3+} . In this graph, only the 0.5% Ho, 10% Gd generated the Gd^{3+} UC emission peak.

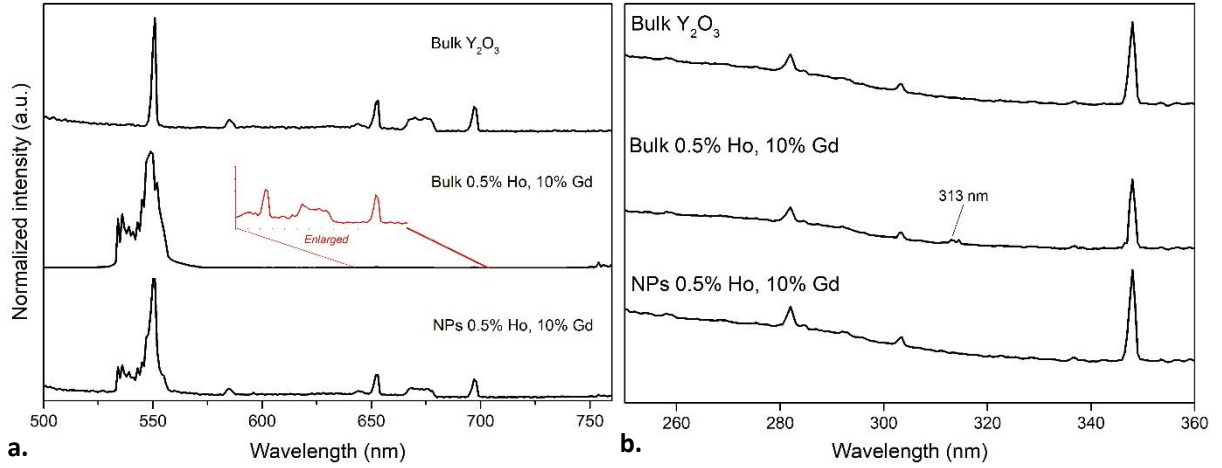


Figure 8.2: CW-laser measurements in **a.** PL emission graphs of microcrystalline and nanocrystalline (Method B) Y_2O_3 : x% Ho, y% Gd samples. **b.** Blue-to-UVB UC of microcrystalline and nanocrystalline Y_2O_3 : x% Ho^{3+} , y% Gd^{3+} samples.

To investigate whether the peaks around the 650-700 nm were generated due to the CW-laser or size of the particles. Emission and blue-to-UVB UC measurements were performed on undoped Y_2O_3 , Ho^{3+} - Gd^{3+} doped Y_2O_3 and for the particles of different sizes. In Figure 8.2 **a.** the emission spectrum of the undoped Y_2O_3 has the same emission of the 5S_2 intermediate state in the 550 nm, and the peaks around the 650-700 nm were observed. In the microcrystalline and nanocrystalline Ho^{3+} - Gd^{3+} doped emission spectra, the familiar shaped 5S_2 was observed with the reoccurring unidentified peaks around the 650-700 nm. The blue-to-UVB UC graph in Figure 8.2 **b.** for the microcrystalline undoped Y_2O_3 has the same noise in the lower UV region and sharp peak at 347 nm as in the bulk and nanocrystalline Ho^{3+} - Gd^{3+} doped Y_2O_3 .

The appearance of the 5S_2 emission peak and the peaks around the 650-700 nm in undoped Y_2O_3 . Confirmed that these peaks were not due to the Ho^{3+} or Gd^{3+} dopants nor due to the size of the particles. This the same case for the blue-to-UVB UC noise and sharp 347 nm peak. Finally, it can be concluded that the discrepancies in the graphs are generated by the CW-laser itself. The CW-laser was not monochromatic which means that these results were unusable.

B. Excitation graphs of 1 & 3% Ho^{3+} concentration

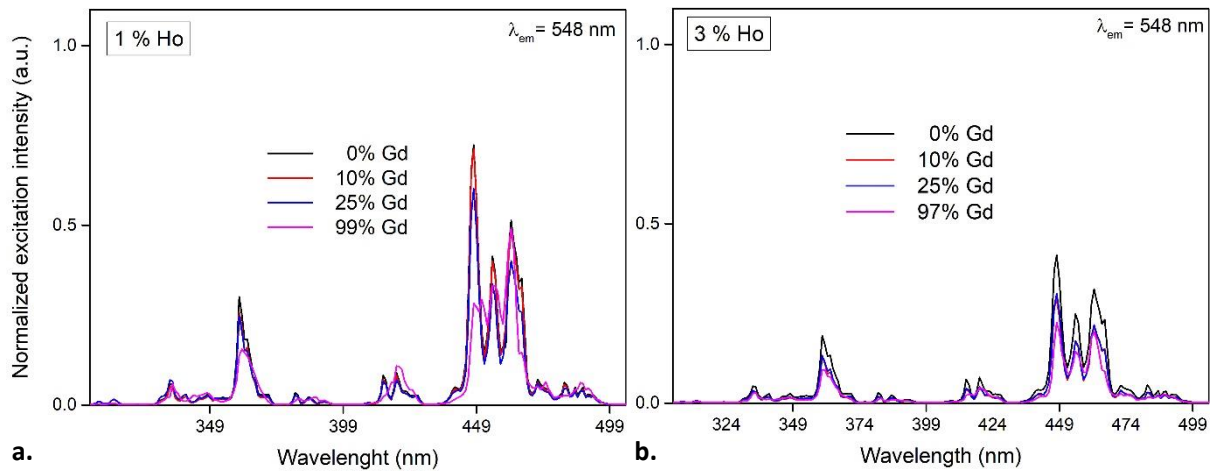


Figure 8.3: Excitation spectra of Y_2O_3 : $x\% \text{Ho}^{3+}$, $y\% \text{Gd}^{3+}$ (with $x= 1$ and 3% , $y = 0, 10, 25$ and 99.5% Gd).

C. TEM images of the NPs of Method B calcined at various temperatures

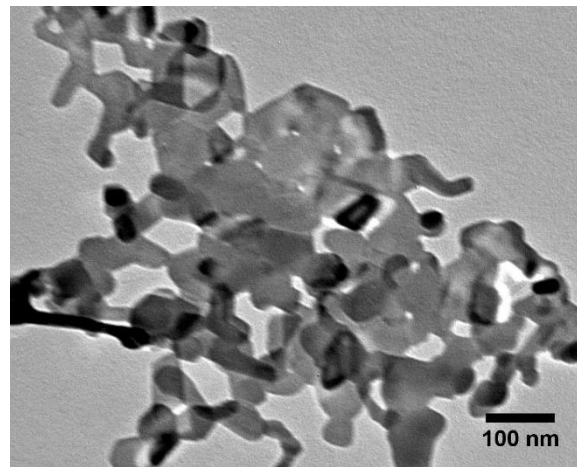


Figure 8.4: Method B Y_2O_3 : 0.5% Ho^{3+} , 10% Gd^{3+} NPs calcined at 900°C for 3 h.

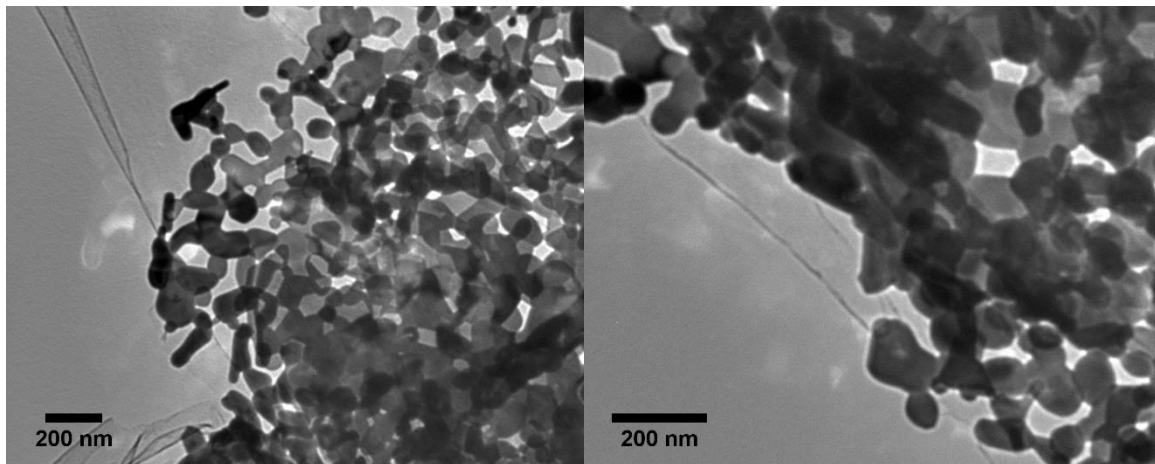


Figure 8.5: Method B Y_2O_3 : 0.5% Ho^{3+} , 10% Gd^{3+} NPs calcined at 1000°C for 3 h.

